Exploring the Structure and Dynamics of Shock/Turbulent Boundary Layer Interactions Generated by Swept Compression Ramps in a Mach 2 Freestream

A Thesis Presented for the

Master of Science

Degree

The University of Tennessee, Knoxville

Daniel S. Allen

May 2023

Distribution is unlimited/AFRL-2023-2280; Cleared 05/11/2023

Copyright © 2023 by Daniel S. Allen.
All rights reserved.

Distribution is unlimited/AFRL-2023-2280; Cleared 05/11/2023

ACKNOWLEDGEMENTS

This work was funded by the Air Force Research Laboratory under contract number FA8650-20-C-2407. I would like to thank Dr. Schmisseur for advising me while handling the mantle of the Executive Director at the University of Tennessee Space Institute (UTSI). Thank you to Dr. Phillip Kreth for training me in many forms of data processing, coding, techniques, and helping me understand concepts of fluid dynamics in general. Thank you to Dr. Kenneth Langley for spending an unthinkable number of hours guiding me through my experiments and data processing, and showing me the light at the end of the (wind) tunnel. Thank you to my coworkers, classmates, and friends at UTSI. Whether it be running experiments, studying together, or attending weekend functions, I would not have been able to get through it all without your help, fellow guidance, and friendship. Thank you to the wind tunnel engineers Kirk Davenport, John Strike, Larry Alexander, and Jonathan Kolwyck for operating our wind tunnels and providing their guidance and assistance when it came to using any data recording equipment. Finally, thank you again to Kirk for helping to produce my experimental models at UTSI.

Distribution is unlimited/AFRL-2023-2280; Cleared 05/11/2023

ABSTRACT

This thesis reports the investigation of the unsteadiness of a 2D and 3D swept shock-wave/turbulent boundary layer interaction (STBLI) and the effect the extent of subsonic flow has on the separation location. Two swept compression ramp cases are investigated at Mach 2 freestream conditions – a high sweep of 30 degrees and a low sweep of 10 degrees both having the same compression angle of 22.5 degrees in the vertical plane. Using a number of diagnostic techniques including stereoscopic and planar particle image velocimetry (PIV) and unsteady pressure sensitive paint (PSP) anchored with pressure transducers, the unsteadiness, the extent of subsonic velocities, and the streamwise point of separation are all measured inside the separation bubble. The differences between the quasi-conical and quasi-cylindrical separation regions resulting from the different sweep cases are further investigated. The subsonic extent and the separation point were found to have a linear correlation with one another, and the correlation decreases with increasing sweep angles from an average correlation coefficient of 0.47 at the lower sweep to 0.33 at the higher sweep. Furthermore, the unsteadiness was found to shift to higher frequencies as the sweep angle increased, with dominant frequencies of approximately 0.7 kHz at the lower sweep and a range of 0.7 to 2.2 kHz at the higher sweep. When increasing the sweep angle, the crossflow velocities approximately tripled from a value of 50 m/s in the lower swept case to a value of 140 m/s in the higher swept case at the boundary layer height of y = 2 mm, and at y = 8 mm the crossflow velocities approximately doubled from 50 m/s to 100 m/s.

Distribution is unlimited/AFRL-2023-2280; Cleared 05/11/2023

TABLE OF CONTENTS

Chapter 1 Introduction 1
1.1 Motivation 1
1.2 Objectives 3
Chapter 2 Literature Review 7
2.1 Shock/Turbulent Boundary Layer Interactions 7
2.1.1 2D and 3D STBLIs 7
2.1.2 Characteristics of STBLI Unsteadiness 11
Chapter 3 Experimental Setup and Procedure 18
3.1 Experimental Facility 18
3.2 Test Article Geometry 18
3.3 Fluorescent Oil Flow Visualization Setup 21
3.4 Particle Image Velocimetry Setup 22
3.4.1 Streamwise-Wall Normal (x-y) Plane Stereoscopic PIV 24
3.4.2 Streamwise-Spanwise (x-z) Planar PIV 26
3.4.3 PIV Data Processing Procedures 26
3.5 Unsteady Pressure Sensitive Paint Anchored with 4 Pressure Transducers 28
3.5.1 Experiment Details 28
3.5.2 Pressure Transducer Data Processing Procedures 29
3.5.3 PSP Data Processing Procedures 29
3.6 Uncertainty Discussion 31
3.6.1 Particle Image Velocimetry 31
3.6.2 Unsteady Pressure Sensitive Paint 32
Chapter 4 Experimental Results 34
4.1 Oil Flow Visualization 34
4.2 Stereoscopic and Planar PIV Results 37
4.2.1 Stereoscopic PIV 37
4.2.2 Planar PIV 44
4.2.3 Comparison and Statistics 50
4.3 Unsteady Pressure Sensitive Paint 61

Distribution is unlimited/AFRL-2023-2280; Cleared 05/11/2023

Chapter 5 Conclusions 70
References 72
Vita 77

Distribution is unlimited/AFRL-2023-2280; Cleared 05/11/2023

LIST OF TABLES

Table 1. Higher-order statistics for subsonic extent of planar PIV Data at y = 2 mm..... 41

Distribution is unlimited/AFRL-2023-2280; Cleared 05/11/2023

LIST OF FIGURES

Figure 1.1. (a) X-15A-2 flight test image (flow left to right) and (b) images taken post-flight test of resulting damage from SBLIs in the blue circles and a shock-shock interaction in the red circle both caused by the ramjet attachment [4]. 2

Figure 1.2. Illustration created by NASA [5] of a scramjet showing SBLIs ubiquitous throughout the engine. 4

Figure 1.3. Image of a sabot breaking away from a high-speed projectile with flow traveling left to right [6]. 5

Figure 2.1. Canonical 2D STBLI configurations featuring: (a) compression ramp, (b) reflected shock, and (c) blunt fin. This schematic was obtained from Clemens and Narayanaswamy [17]. 8

Figure 2.2. Schematic obtained from Settles and Teng [25] showing the characteristics of (a) cylindrically symmetric low sweep SBLI and (b) quasi-conically symmetric high sweep SBLI over a swept compression ramp. 10

Figure 2.3. Power spectral densities from Erengil and Dolling [20] of pressure transducers showing evolution to higher frequency peaks as the sweepback denoted as λ_c increases. 13

Figure 2.4. RANS simulation by Holst and Schmisseur [37] showing streamwise slices of the subsonic extent at varying spanwise points of a (a) 10° λ_{sweep} and (b) 30° λ_{sweep} interaction. 15

Figure 2.5. Very thorough LES simulation showing a 3D rendering of interactions with 30° sweep and 22.5° compression angle performed by Adler and Gaitonde [36]. The shock is represented in blue. 16

Figure 3.1. UTSI Mach 2 blowdown tunnel schematic. 19

Figure 3.2. (a) 10° (top) and 30° (bottom) λ_{sweep} models and mounting floor insert (right) were 3D-resin printed. (b) CAD model of a swept compression ramp positioned inside UTSI Mach 2 blowdown tunnel. Waves emanating from alignment imperfections are also shown. 20

Distribution is unlimited/AFRL-2023-2280; Cleared 05/11/2023

Figure 3.3. Schematic of the oil flow visualization experiment from a (a) top-down perspective and (b) side perspective. The orange lines are where the oil flow is applied before a run begins. 23
Figure 3.4. a) Diagram of the configuration for stereo PIV. b) Photo of experimental setup for stereo PIV. 25
Figure 3.5. a) Diagram of the configuration for planar PIV. b) Photo of experimental setup for planar PIV. 27
Figure 3.6. Photo of uPSP experimental setup with PSP coat applied onto 30° λ_{sweep} model. 30
Figure 4.1. Fluorescent oil flow showing quasi-cylindrical symmetry between the boundary layer separation line and reattachment line of the boundary layer around the separation region of the 10° λ_{sweep} compression ramp. 35
Figure 4.2. Fluorescent oil flow showing quasi-conical symmetry between the boundary layer separation line and reattachment line of the boundary layer around the separation region of the 30° λ_{sweep} compression ramp. 36
Figure 4.3. Stereoscopic PIV results for 30° λ_{sweep} showing (a) the ensemble-averaged velocity magnitude and (b) the standard deviation of the velocity magnitude. 38
Figure 4.4. Stereoscopic PIV results for 10° λ_{sweep} showing (a) the ensemble-averaged velocity magnitude and (b) the standard deviation of the velocity magnitude. 39
Figure 4.5. a) Turbulent boundary layer velocity profile and b) Van-Driest velocity transform at x/δ_{99} = -3 for the 30° λ_{sweep} case 40
Figure 4.6. a) Turbulent boundary layer velocity profile and b) Van-Driest velocity transform at x/δ_{99} = -3 for the 10° λ_{sweep} case 41
Figure 4.7. Stereoscopic PIV results for the ensemble-averaged crossflow velocity field for (a) the 30° λ_{sweep} and (b) the 10° λ_{sweep}. 43
Figure 4.8. 30° λ_{sweep} planar PIV, ensemble-averaged velocity magnitudes with a streamwise wall-normal laser sheet at: (a) y = 2 mm, (b) y = 4.5 mm, and (c) y = 8 mm. 45

Distribution is unlimited/AFRL-2023-2280; Cleared 05/11/2023

Figure 4.9. 10° λ_{sweep} planar PIV, ensemble-averaged velocity magnitudes with a streamwise wall-normal laser sheet at: (a) y = 2 mm, (b) y = 4.5 mm, and (c) y = 8 mm. 46
Figure 4.10. 30° λ_{sweep} planar PIV, ensemble-averaged crossflow velocity field with a streamwise wall-normal laser sheet. (a) y = 2 mm, (b) y = 4.5 mm, and (c) y = 8 mm. 48
Figure 4.11. 10° λ_{sweep} planar PIV, ensemble-averaged crossflow velocity field with a streamwise wall-normal laser sheet. (a) y = 2 mm, (b) y = 4.5 mm, and (c) y = 8 mm. 49
Figure 4.12. Ensemble-averaged uncertainty field of the stereoscopic PIV results for a) 30° λ_{sweep} and b) 10° λ_{sweep}. 51
Figure 4.13. Ensemble-averaged uncertainty field of the 30° λ_{sweep} planar PIV results for a) y = 2 mm, b) y = 4.5 mm, and c) y = 8 mm. 52
Figure 4.14. Ensemble-averaged uncertainty field of the 10° λ_{sweep} planar PIV results for a) y = 2 mm, b) y = 4.5 mm, and c) y = 8 mm. 53
Figure 4.15. Combined planar and stereoscopic PIV figures for (a) 30° λ_{sweep} and (b) 10° λ_{sweep}. 54
Figure 4.16. Histograms of the subsonic extent along a streamwise plane leading up to the compression corner located along (a) z/δ_{99} = -0.5, (b) z/δ_{99} = 0, and (c) z/δ_{99} = 0.5 for 30° λ_{sweep} in the y = 2 mm planar PIV results. 56
Figure 4.17. Histograms of the subsonic extent along a streamwise planes leading up to the compression corner located along (a) z/δ_{99} = -0.5, (b) z/δ_{99} = 0, and (c) z/δ_{99} = 0.5 for 10° λ_{sweep} in the y = 2 mm planar PIV results. 57
Figure 4.18. Scatter plots comparing the separation location and the subsonic extent in the planar PIV y = 2 mm case at (a) z/δ_{99} = -0.5, (b) z/δ_{99} = 0, and (c) z/δ_{99} = 0.5 for 30° λ_{sweep}. 58
Figure 4.19. Scatter plots comparing the separation location and the subsonic extent in the planar PIV y = 2 mm case at (a) z/δ_{99} = -0.5, (b) z/δ_{99} = 0, and (c) z/δ_{99} = 0.5 for 10° λ_{sweep}. 59

Distribution is unlimited/AFRL-2023-2280; Cleared 05/11/2023

Figure 4.20. PSP pressure fields for (a) case 1 and (b) case 2 along with the (c) P'_{rms} values in psi at 30° λ_{sweep}. 62
Figure 4.21. PSP pressure fields for (a) case 1 and (b) case 2 along with the (c) P'_{rms} in psi values at 10° λ_{sweep}. 63
Figure 4.22. Trace of the PSP-computed P'_{rms} values for (a) 30° λ_{sweep} and (b) 10° λ_{sweep} calculated along a horizontal line located at z/δ_{99} = 0.49 (directly below the line of pressure taps). 64
Figure 4.23. Case 1 for the 30° λ_{sweep}: (a) PSDs of P' values from PSP images investigated directly below each pressure tap for tap positions 1 and 3, and (b) PSDs of the Kulite transducers. 66
Figure 4.24. Case 2 for the 30° λ_{sweep}: (a) PSDs of P' values from PSP images investigated directly below each pressure tap for tap positions 2 and 4, and (b) PSDs of the Kulite transducers. 67
Figure 4.25. Case 1 for 10° λ_{sweep}: (a) PSDs of P' values from PSP images investigated directly below each pressure tap for tap positions 1 and 3, and (b) PSDs of the Kulite transducers. 68
Figure 4.26. Case 2 for 10° λ_{sweep}: (a) PSDs of P' values from PSP images investigated directly below each pressure tap for tap positions 2 and 4, and (b) PSDs of the Kulite transducers. 69

Distribution is unlimited/AFRL-2023-2280; Cleared 05/11/2023

CHAPTER 1
INTRODUCTION

1.1 Motivation

Shock-wave boundary layer interactions, or SBLIs, are universally present on supersonic vehicles and can be unsteady causing large thermomechanical loads on the surface of the vehicle [1,2]. SBLIs create uncertainty in vehicle design when it comes to the survivability of these vehicles during flight, and the locations of these interactions along with their unsteadiness have been of significant interest in the aerospace community since the 1940s [2]. SBLIs are notably located on important flow control surfaces such as fins, ailerons, engine nozzles and inlets which has a detrimental effect on the ability and efficiency to control the flow around the vehicle and within the engine. SBLIs are typically the source of the highest average and fluctuating thermal and pressure loads experienced on a vehicle. Understanding what drives the unsteadiness of the shock foot can result in the ability to control where these high loads are experienced, or even reduce the strength of these interactions. This would improve vehicle design through durability and weight control which is especially integral in the supersonic and hypersonic speed regimes where the greatest challenge is ensuring a vehicle, including electronic equipment and passengers, can survive until it reaches its destination [3].

One of the earliest examples regarding the importance of understanding SBLIs and the impact these interactions can have on a vehicle is the flight test results of the X-15A-2 when a dummy ramjet was carried under the fuselage at Mach 6.7 at high altitude [3]. The vehicle shown in Figure 1.1 (a) experienced an SBLI which burned bare through the surface of the ablative coating with the resulting damage shown in Figure 1.1 (b) circled in blue on the bottom of the fuselage where the ramjet was placed thus signifying the beginning of the United

Distribution is unlimited/AFRL-2023-2280; Cleared 05/11/2023

a)



b)

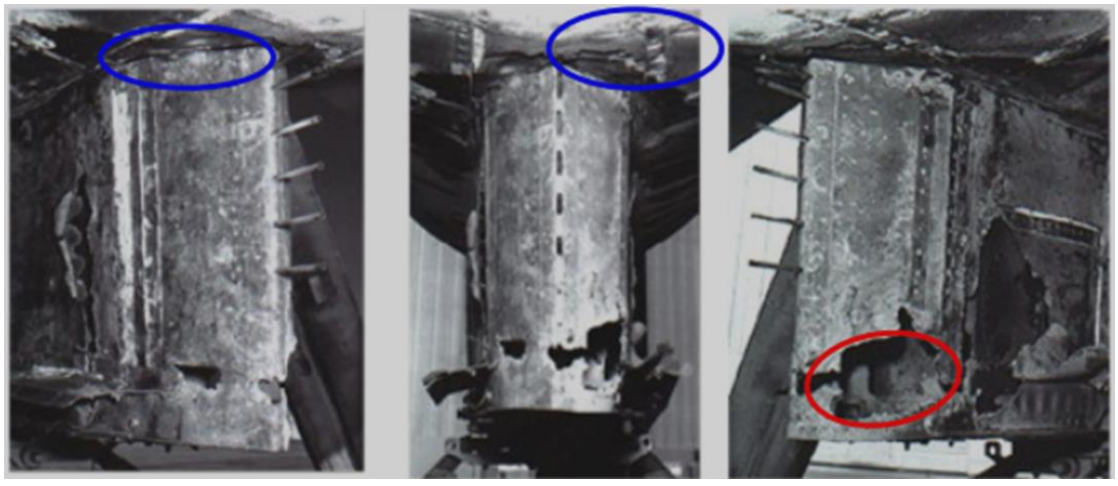


Figure 1.1. (a) X-15A-2 flight test image (flow left to right) and (b) images taken post-flight test of resulting damage from SBLIs in the blue circles and a shock-shock interaction in the red circle both caused by the ramjet attachment [4].

Distribution is unlimited/AFRL-2023-2280; Cleared 05/11/2023

States interest in SBLI research [4]. Another source of interest for advancements in SBLI research is NASA stating that higher performing air-breathing engines requires a better understanding of flow environments that SBLIs dominate such as inlets and nozzles as seen in Figure 1.2 [4]. The U.S. Army faces challenges regarding SBLIs occurring over high-speed, antiarmor, kinetic energy penetrators that fly between Mach 4 to Mach 8 at sea level conditions [2] shown in Figure 1.3 where the sabot breaks away from the high-speed projectile [5], and thus, 3D SBLIs are instantaneously present as they travel over these complex geometries.

1.2 Objectives

This study is a follow-up of a SciTech paper by Allen et. al [7] using the same experimental data as was taken in the conference paper, but this thesis features more strenuous data processing and an analysis of deeper scrutiny with higher fidelity and better-resolved results. The ultimate goal of the present research effort is to provide simple guidelines for structural design around control systems and to provide a highly-resolved data set for the assessment of industrial and design-oriented simulation capabilities by further characterizing 3D and 2D shock/turbulent boundary layer interactions (STBIs) along with a comparison of the two cases. This thesis contains two specific goals. The first of which is to understand how subsonic flow within the separation bubble affects the unsteadiness of an ‘open’ 3D and ‘closed’ approximately 2D STBLI over a swept compression ramp (SCR). The second goal is to compare the ‘open’ and ‘closed’ separation bubbles found before highly swept and low swept compression ramps, respectively. Herein, experiments are presented in a Mach 2 freestream that quantitatively characterize the flow over two separate compression ramps with a vertical angle of 22.5°: one with a low sweep (10°) and one with a high sweep (30°). Multiple optical diagnostic techniques are used to drive a more thorough understanding of the flow physics including fluorescent oil flow, stereoscopic and

Distribution is unlimited/AFRL-2023-2280; Cleared 05/11/2023

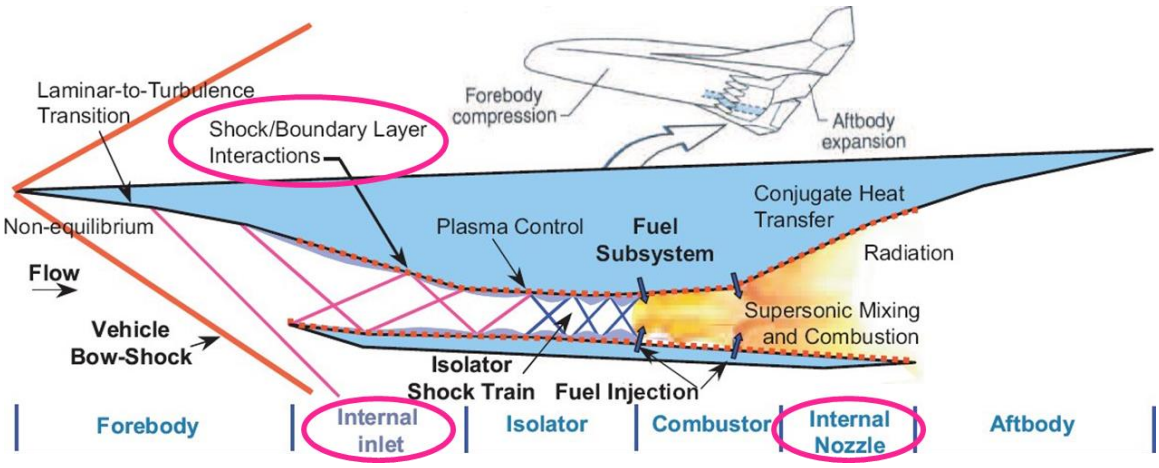


Figure 1.2. Illustration created by NASA [5] of a scramjet showing SBLIs ubiquitous throughout the engine.

Distribution is unlimited/AFRL-2023-2280; Cleared 05/11/2023

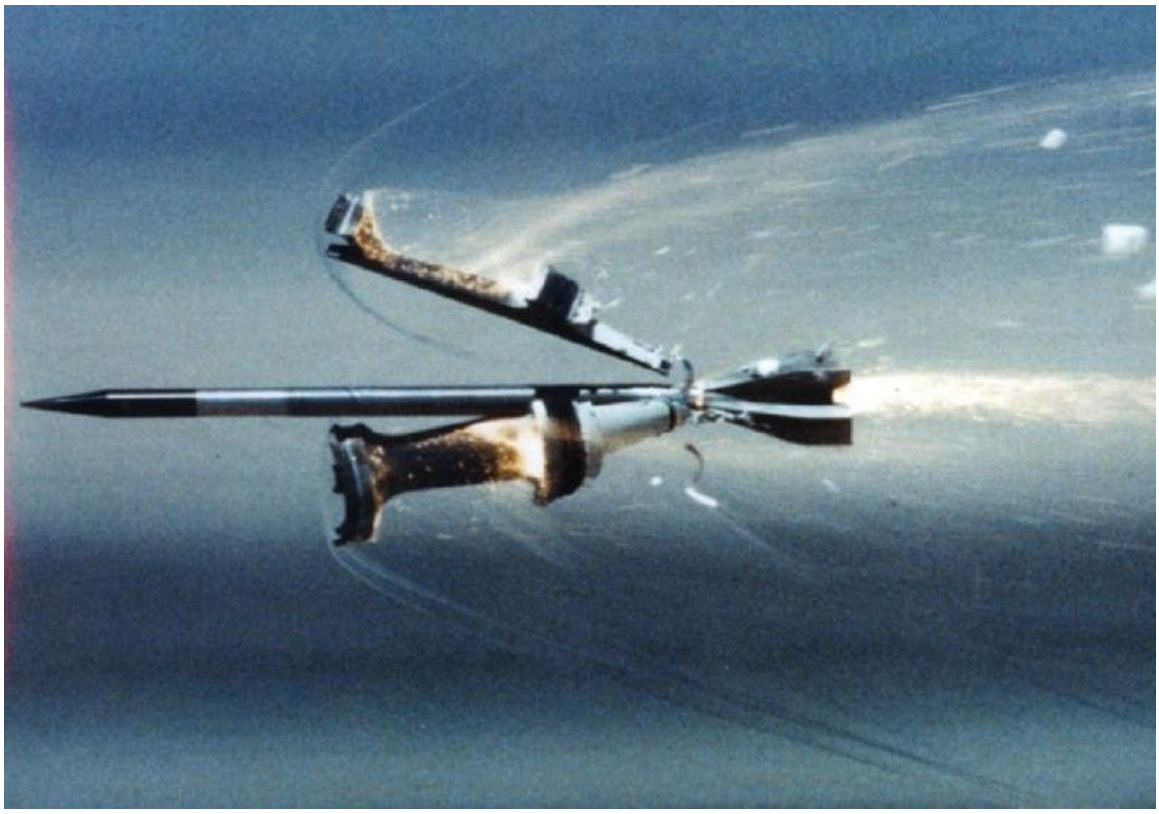


Figure 1.3. Image of a sabot breaking away from a high-speed projectile with flow traveling left to right [6].

Distribution is unlimited/AFRL-2023-2280; Cleared 05/11/2023

planar particle image velocimetry (PIV), and unsteady pressure sensitive paint (uPSP). At the onset, the hypothesis of this study was that the frequency of the unsteadiness for these STBLIs are correlated with the extent of subsonic flow within the interaction. Since downstream perturbations are capable of traveling upstream in subsonic flow, the streamwise location of the separation shock can be affected by those downstream perturbations. This thesis further hypothesizes that a high subsonic extent causes a larger intermittent region and lower frequency of the STBLI, whereas a low subsonic extent causes a small intermittent region and a higher frequency.

Distribution is unlimited/AFRL-2023-2280; Cleared 05/11/2023

CHAPTER 2
LITERATURE REVIEW

2.1 Shock/Turbulent Boundary Layer Interactions

Shock/turbulent boundary layer interactions, or STBLIs, are a specific subset of SBLIs where the interacting boundary layer is fully developed turbulent flow and the shock-induced separation can exhibit inherent unsteadiness. Characteristics of an STBLI are the significant unsteadiness and deformation of the shock wave, and the turbulence experiences a notable change in the characteristic velocity, time scales, and length scales [8]. Andreopoulos et. al [8] report that the effects of the STBLI depend on many aspects of the shock wave such as strength, orientation, position, and shape. However, it is important to note that the unsteadiness, along with its mechanical loading, is the dominating phenomenon in many flow fields [2] which shows that controlling where this unsteadiness occurs should be a priority.

2.1.1 2D and 3D STBLIs

The two types of STBLIs that are the focus of this research are spanwise-homogeneous, or 2D, STBLIs and spanwise-nonhomogeneous, or 3D, STBLIs. 2D STBLIs have been studied and characterized broadly [8-20]. A schematic created by Clemens and Narayanaswamy [17] of three canonical 2D STBLIs can be seen in Figure 2.1. However, spanwise-nonhomogeneous 3D interactions over control surfaces such as swept ramps and fins may have different drivers of unsteadiness when considering the mass relief effect due to spanwise flow [20]. 3D STBLIs have received large attention over the last few decades [20-39], but there is still a great deal to be discovered about their characteristics and unsteadiness drivers. A 2D interaction is characterized as a separation occurring

Distribution is unlimited/AFRL-2023-2280; Cleared 05/11/2023

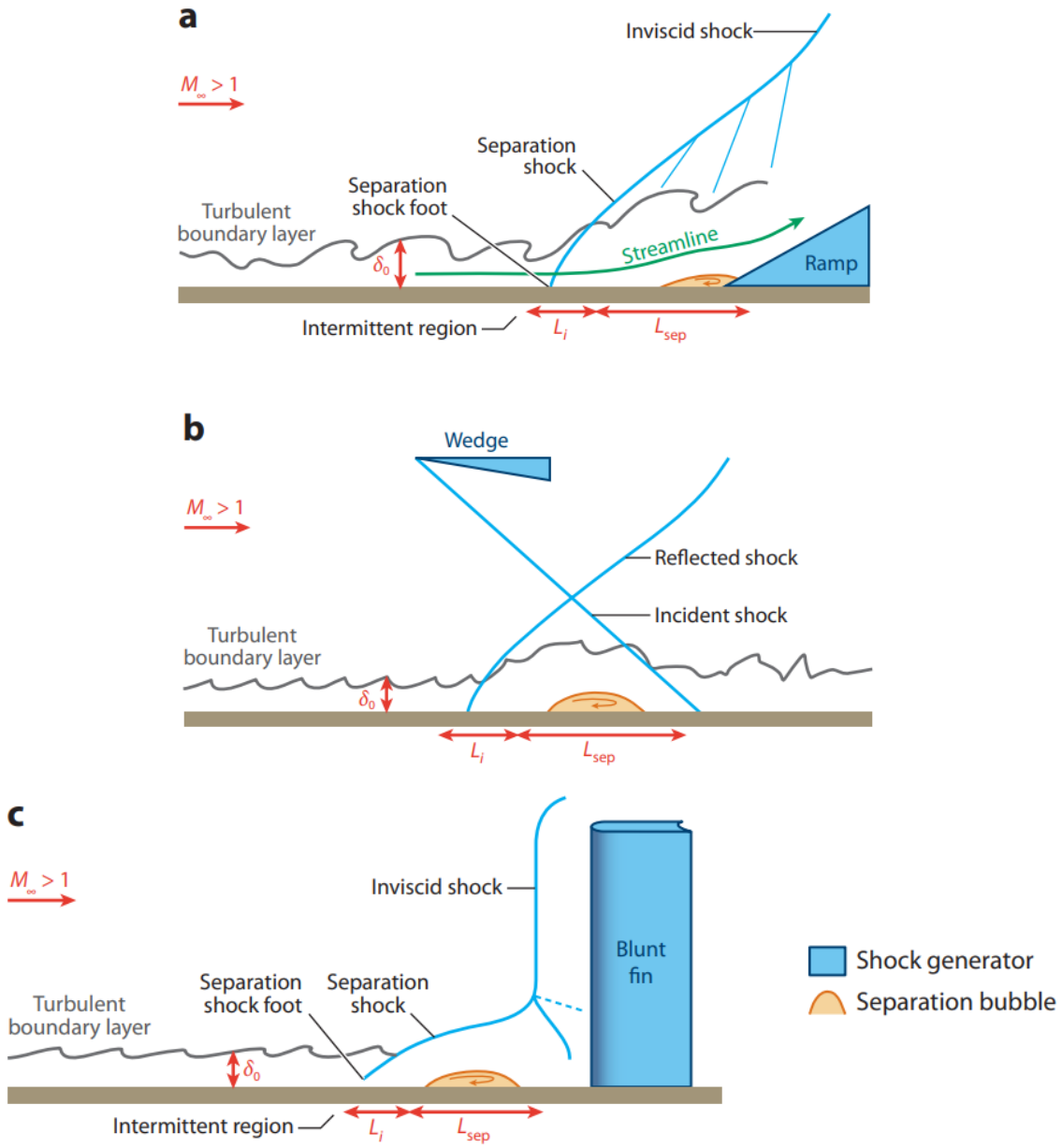


Figure 2.1. Canonical 2D STBLI configurations featuring: (a) compression ramp, (b) reflected shock, and (c) blunt fin. This schematic was obtained from Clemens and Narayanaswamy [17].

Distribution is unlimited/AFRL-2023-2280; Cleared 05/11/2023

in a single plane where there is no crossflow along the span; thus, the fluid's mass is trapped in a 'closed' 2-dimensional recirculation bubble. When crossflow along the span is introduced, out-of-plane mass flows in and out of the separation bubble generating 3D effects. These 3D interactions are referred to as having 'open' separation bubbles. Understanding the difference between characteristics of the 2D unsteadiness with low crossflow present and characteristics of the 3D unsteadiness with high crossflow present will better help engineers design effective flight vehicles.

Some canonical examples of 2D STBLIs are unswept cases of impinging shock-induced separation [13-17] as shown in Figure 2.1 (b) and shock-induced separation caused by incoming flow over an unswept compression ramp [9-12,18-20] as shown in Figure 2.1 (c). Shock-induced turbulent separation typically features a separation shock that exhibits low-frequency, large-scale motion. The frequency is low relative to the high turbulent eddy frequency found in the incoming boundary layer flow, and the large-scale motion results from the shock foot fluctuating in the streamwise direction on the order of several boundary layer thicknesses, δ_{99}, with the length being contingent upon the model geometry tested [9]. Using pressure transducers in the separation region upstream of an unswept compression ramp, Erengil and Dolling [9] report the separation bubble expanding and contracting with respect to large- and small-scale separation, and records that there is a correlation between the separation shock foot motion and the low-frequency pressure fluctuations of the separation bubble.

The two cases of interest in this paper are that of a high sweep compression ramp and a low sweep compression ramp at a given vertical compression angle, where the boundary between these two cases is considered $\lambda_{sweep} \geq 25°$ and $\lambda_{sweep} < 25°$, respectively [20]. A high sweep condition of 30° has been considered in several prior studies [20,25,27-38], while the low sweep condition of 10° has not been as widely reported [20]. Figure 2.2 from Settles and Teng [25] show the different characteristics of a low and high sweep SBLI ahead of a swept

Distribution is unlimited/AFRL-2023-2280; Cleared 05/11/2023

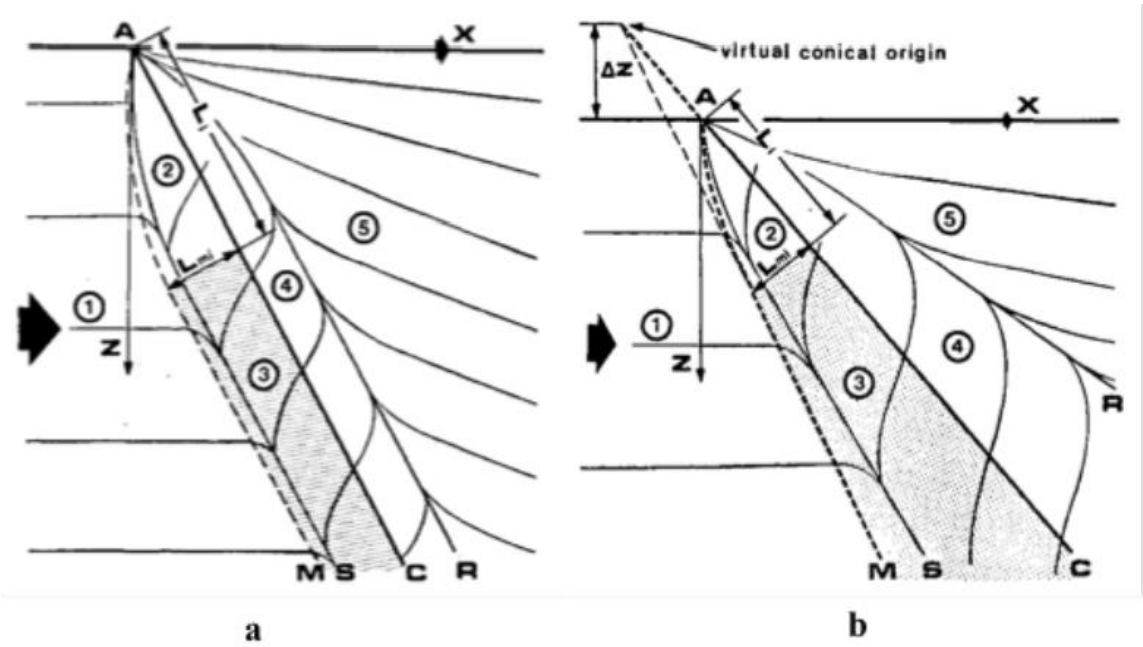


Figure 2.2. Schematic obtained from Settles and Teng [25] showing the characteristics of (a) cylindrically symmetric low sweep SBLI and (b) quasi-conically symmetric high sweep SBLI over a swept compression ramp.

Distribution is unlimited/AFRL-2023-2280; Cleared 05/11/2023

compression ramp. In a low sweep case, the separation line, compression ramp corner, and reattachment line appear to be cylindrically symmetric to one another after reaching the spanwise inception point away from the apex of the leading edge where the symmetry is fully developed [25]. These cylindrically symmetric interactions share some characteristics with 2D interactions since there is not as strong of crossflow and will be treated as 2D interactions in the experiments reported here. In a high sweep case, the separation and reattachment lines are quasi-conically symmetric relative to the compression corner after the inception point, featuring a virtual conical origin (VCO) that both lines can be traced back to from the fully developed symmetry [25]. However, it is important to note that Vanstone, et al. [29] propose that the low sweep case actually features a very weak quasi-conical symmetry instead of cylindrical symmetry.

2.1.2 Characteristics of STBLI Unsteadiness

Prior studies have shown the separation shock foot position to be directly correlated to and driven by the fullness of the boundary layer velocity profile, with smaller separation regions due to fuller boundary layers and vice versa, using diagnostic techniques such as planar particle image velocimetry and high-frequency wall pressure measurements over an unswept ramp at Mach 5 [10]. As for unsteadiness, Beresh, et al. [10] concluded that upstream boundary layer velocity fluctuations are related to the motion of the separation shock foot and are a significant source of a turbulent SBLI's unsteadiness. A number of other studies came to the same conclusion following Ref. [10] with respect to 2D STBLIs [11-12,15,17-19]. For the 3D STBLI, a correlation between the separation location and the momentum of the boundary layer, with high momentum boundary layers correlated to a smaller separation region and vice versa, was also observed over a 30° swept ramp at Mach 2 with a compression angle of 22.5° by using stereoscopic particle image velocimetry [28].

Distribution is unlimited/AFRL-2023-2280; Cleared 05/11/2023

Erengil and Dolling [20] report on unsteadiness investigations that were conducted over compression ramps at varying sweep angles from unswept to λ_{sweep} of 10°, 20°, 25°, 30°, 40°, and 50° at Mach 5 conditions with a compression angle of 28°. Using a large number of pressure taps traversing through the start of the separation region and nearing the compression corner along a line oriented normal to the sweep angle of a given case, they found that the length of the intermittent region (characterized as the range that the separation shock foot moves) decreases with increasing sweep. This indicates that low-frequency, high-amplitude unsteadiness 'breathing' evolves into high-frequency, low-amplitude 'jitter' as sweepback increases as shown in Figure 2.3. The shock frequencies for a given sweep angle were also reported to have decreased in the spanwise direction due to the intermittent region increasing in size.

Over the last decade, Vanstone has performed a number of research campaigns [27-32] to further the understanding of the flow structure and large-scale unsteadiness of 3D STBLIs over the 30° swept compression ramp model. These efforts heavily influenced this current research and were the basis of comparison in literature for many of the results found later in this paper. However, Vanstone et. al [28] note that, even though the incoming boundary layer momentum was discovered to drive the unsteadiness of the separation line, the drivers of the unsteadiness are likely complex and varied and there possibly may be many differing driving mechanisms undiscovered. Vanstone et. al [31] reports that the separation and reattachment locations were mostly uncorrelated, the separation region did not show a strong breathing motion, and the separation unsteadiness was greatly affected by incoming boundary layer velocity fluctuations. Vanstone et. al [32] reports that the shock and separation lines characteristically behave differently to one another and possibly explains why there are almost incomparable results among many STBLI studies as many of them use one characterizing feature and state that future work researching two

Distribution is unlimited/AFRL-2023-2280; Cleared 05/11/2023

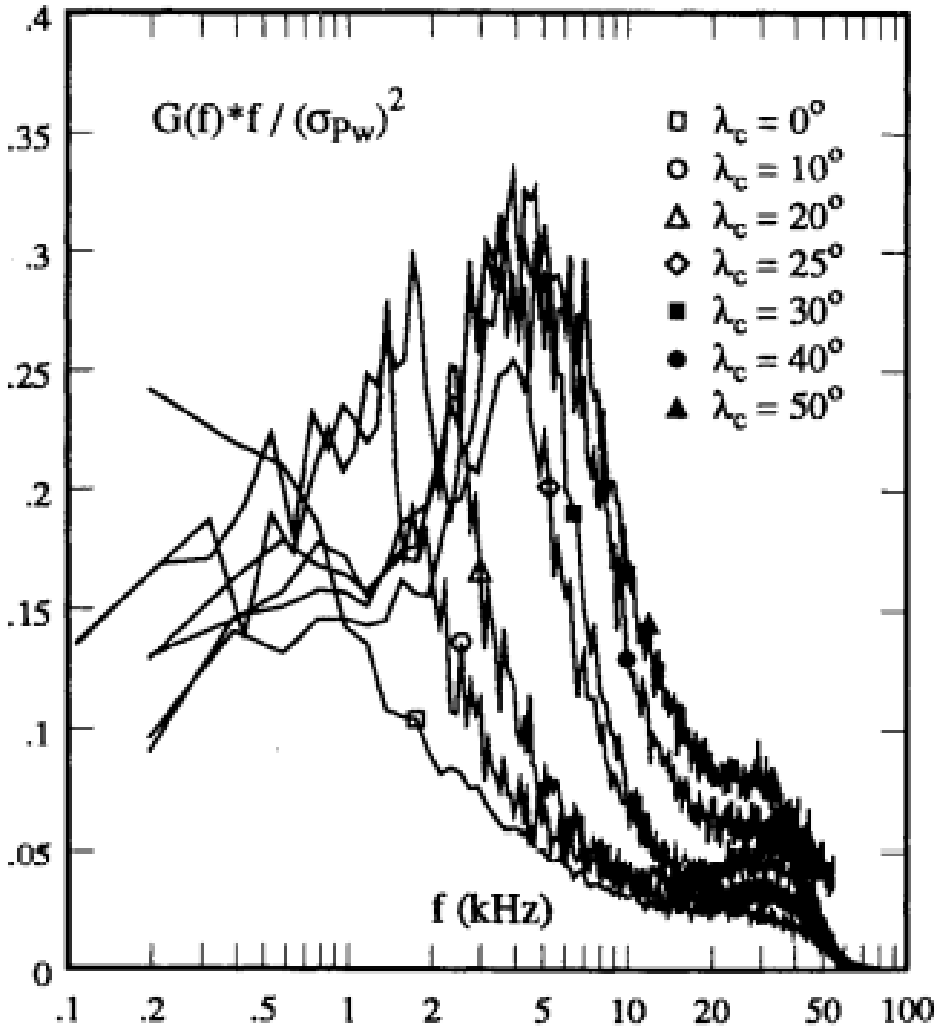


Figure 2.3. Power spectral densities from Erengil and Dolling [20] of pressure transducers showing evolution to higher frequency peaks as the sweepback denoted as λ_c increases.

Distribution is unlimited/AFRL-2023-2280; Cleared 05/11/2023

characterizing features simultaneously could provide an explanation for the better understanding of the SBLI dynamics.

Computational studies have been conducted for 30° sweep compression ramps [33-37] and compared with previous experimental research. Holst and Schmisseur [37] computed Reynolds-averaged Navier-Stokes (RANS) simulations matching the experimental conditions from Refs. [20,27,28] but found that the 3D STBLI stressed the RANS methodologies, indicating that other hybrid approaches may be required for these complex 3D cases. Figure 2.4 from Holst and Schmisseur [37] shows the extent of subsonic flow in streamwise slices of the separation region along different spanwise points. A primary vortex traveling spanwise along the compression corner was noted to be entirely subsonic in the low sweep case and supersonic in the high sweep case. A subsonic vortex allows transmission of downstream perturbations upstream along the entire separation region, whereas a supersonic vortex does not permit upstream transmission [37]. Adler and Gaitonde [36] computed a very thorough investigation, as seen in Figure 2.5, using large-eddy simulations (LES) to compute flow conditions similar to Refs. [27,37] but with compression angles of 22.5°, 30°, and 37.5° to examine the dynamics of unsteady phenomena. Adler and Gaitonde [36] show that the unsteady dynamics of ‘open’ separations differ from ‘closed’ separations, and that reverse streamwise flow is not a good indicator of the unsteady dynamics of ‘open’ separations in contrast to it being indicative of unsteadiness in ‘closed’ separations. LES was further employed to understand the differences in unsteadiness of 3D interactions compared to 2D interactions [34,35]. Adler and Gaitonde [35] compared 2D and 3D interactions and found that the properties of quasi-conical symmetry, strong separated crossflow, and open flow separation are coupled to one another and inherent to 3D interactions. This study also concluded that the thickness of the inner shear layer of the separated flow grows linearly as it is displaced further from the VCO similar to conical symmetry, and the outer

Distribution is unlimited/AFRL-2023-2280; Cleared 05/11/2023

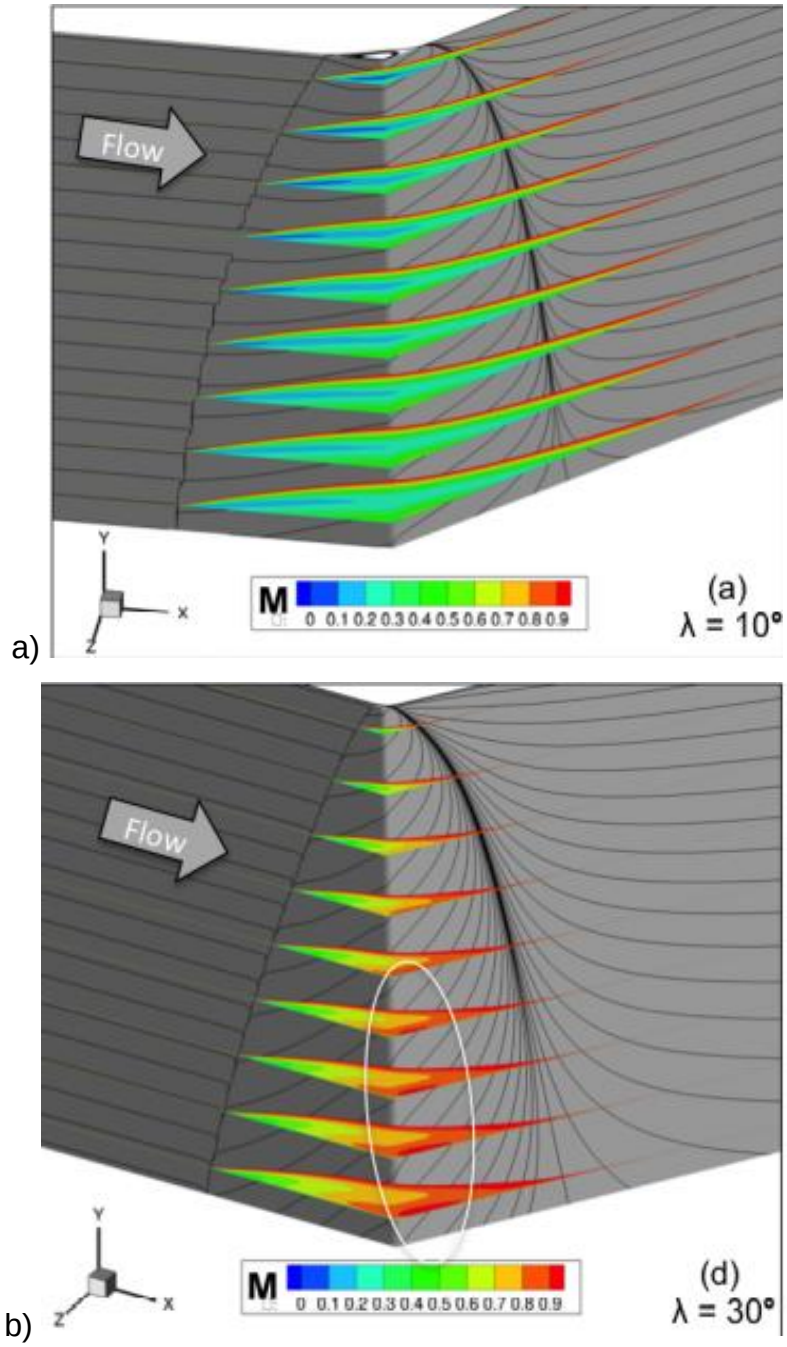


Figure 2.4. RANS simulation by Holst and Schmisseur [37] showing streamwise slices of the subsonic extent at varying spanwise points of a (a) 10° λ_{sweep} and (b) 30° λ_{sweep} interaction.

Distribution is unlimited/AFRL-2023-2280; Cleared 05/11/2023

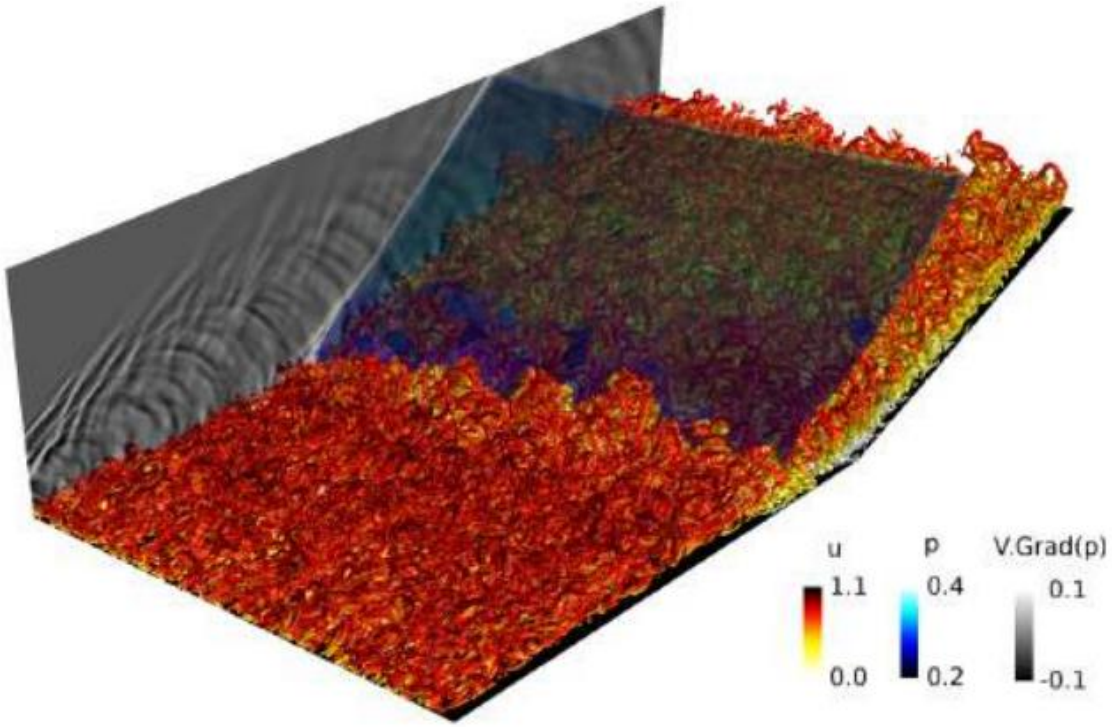


Figure 2.5. Very thorough LES simulation showing a 3D rendering of interactions with 30° sweep and 22.5° compression angle performed by Adler and Gaitonde [36]. The shock is represented in blue.

Distribution is unlimited/AFRL-2023-2280; Cleared 05/11/2023

shear layer grows independently of the displacement of the VCO similar to spanwise homogeneous symmetry [35].

Distribution is unlimited/AFRL-2023-2280; Cleared 05/11/2023

CHAPTER 3
EXPERIMENTAL SETUP AND PROCEDURE

3.1 Experimental Facility

The experiments, which are the same as reported in Allen et. al [7], were conducted in the low-enthalpy, Mach 2 blowdown wind tunnel at the University of Tennessee Space Institute (UTSI). Figure 3.1 displays a solid model representation of the wind tunnel. The stilling chamber pressure is regulated to approximately 210 kPa (or 30.5 psi), and the facility exhausts to atmospheric conditions after the air passes through a diffuser [40]. The average stagnation temperature of the unheated air is approximately 285 K. The test section has a square cross section measuring 8” x 8” (203 mm x 203 mm), with optical access capabilities on the ceiling, floor, and walls. The floor insert is 13” x 3” (330 mm x 76 mm) where the models are mounted on a 5.5” x 2” (140 mm x 51 mm) insert adapter. The incoming boundary layer attached to the test section floor has a thickness, δ_{99}, of 11 mm. The average freestream velocity V_∞ is 507 m/s, which results in a freestream Mach number M_∞ = 2.01 and unit Reynolds number Re = 3.0 x 10^7 m^{-1}. This tunnel can operate at steady state conditions for more than 30 seconds.

3.2 Test Article Geometry

Two swept compression ramp (SCR) models, shown in Figure 3.2 (a), were produced on a resin 3D printer. Both SCRs had a 5” span, a 22.5° compression angle, and a ramp height of 0.75” but featured different sweep angles. The highly swept case had a 30° sweep angle while the other model had a low sweep angle of 10°. A sharp fence was placed on the upstream side of each model protruding

Distribution is unlimited/AFRL-2023-2280; Cleared 05/11/2023

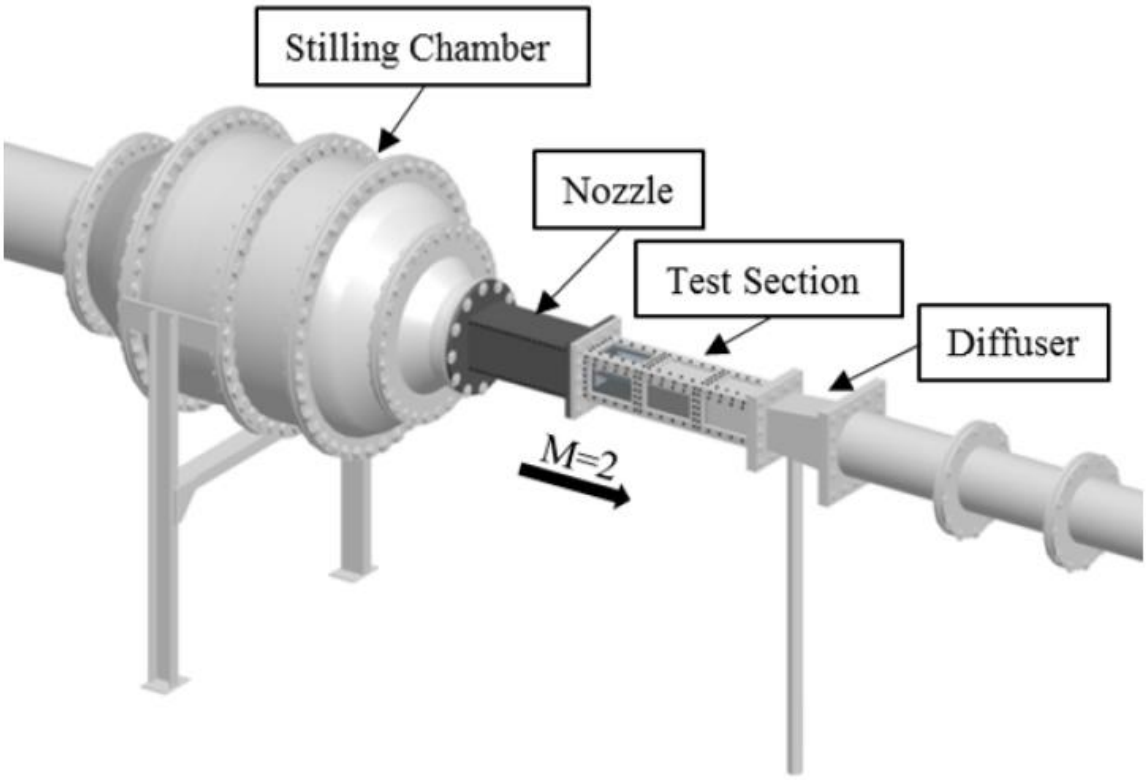


Figure 3.1. UTSI Mach 2 blowdown tunnel schematic.

Distribution is unlimited/AFRL-2023-2280; Cleared 05/11/2023

a)



b)

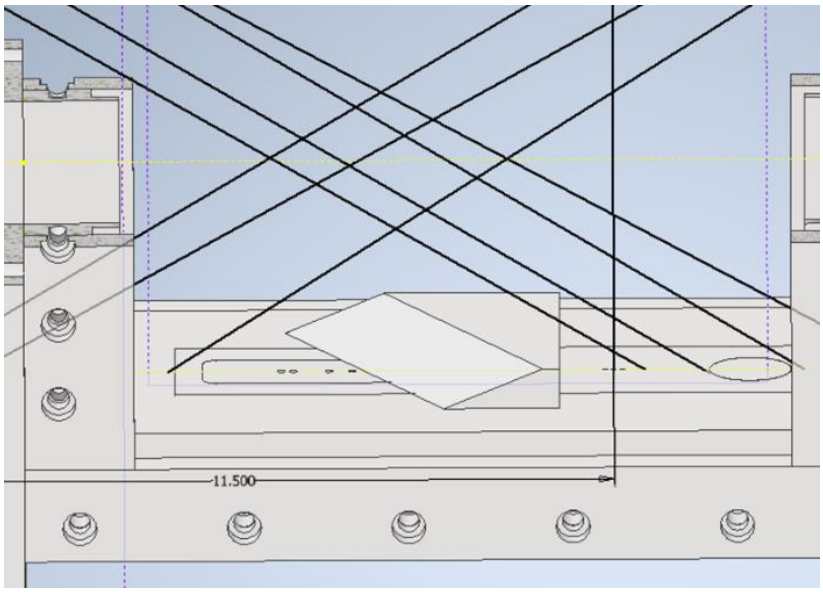


Figure 3.2. (a) 10° (top) and 30° (bottom) λ_{sweep} models and mounting floor insert (right) were 3D-resin printed. (b) CAD model of a swept compression ramp positioned inside UTSI Mach 2 blowdown tunnel. Waves emanating from alignment imperfections are also shown.

Distribution is unlimited/AFRL-2023-2280; Cleared 05/11/2023

0.75” upstream of the apex of each SCR to prevent flow from spilling over the edge. These models were designed such that the centerline edges of the ramps were in the same position in the test section to prevent realignment of the diagnostic equipment. The positioning of the models inside the wind tunnel was determined by avoiding locations where impinging characteristic shocks or misalignment waves interact with these models or their separation regions, and Figure 3.2 (b) shows the location of the model in the test section with black lines representing these waves characteristic to the tunnel along the centerline emanating from upstream to downstream. The inviscid oblique shock strength over the swept models were calculated to assess the interaction strength using Eqs. (3.1) and (3.2). M_{n1} is the incoming Mach component normal to the oblique shock and M_1 is the incoming freestream Mach number. The sine and cosine components are the normal components to the swept oblique shock where β_c is the oblique shock deflection angle for the 22.5° compression angle and λ_s is the sweep angle of the ramp. γ is the specific gas constant of air at a value of 1.4, and P_2/P_1 is the inviscid shock strength of the interaction.

$$M_{n1} = M_1 \sin\beta_c \cos\lambda_s \tag{3.1}$$

$$P_2/P_1 = 1 + \frac{2\gamma}{\gamma+1}(M_{n1}{}^2 - 1) \tag{3.2}$$

The resulting P_2/P_1 values were 3.26 for the 10° sweep, 2.48 for the 30° sweep, and for reference 3.36 for an unswept case. With the relief effect due to the addition of crossflow, the shock strength decreases with increasing sweep values.

3.3 Fluorescent Oil Flow Visualization Setup

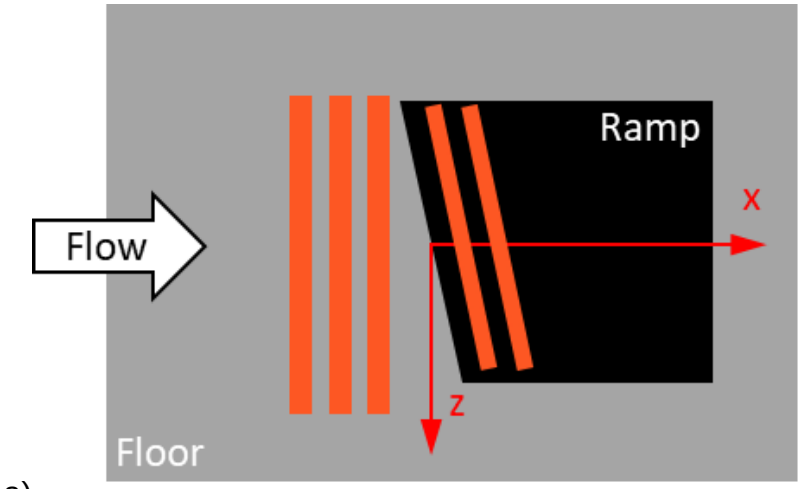
Distribution is unlimited/AFRL-2023-2280; Cleared 05/11/2023

In order to observe the location of the average separation line on the floor leading up to the swept ramp and the average reattachment line on the surface of the swept ramp, fluorescent oil flow was conducted along the test section floor and the model surface. A schematic of the experiment can be seen in Figure 3.3. Fluorescent Rocket Red pigment dye and heavy mineral oil were mixed in a ratio of 1:1 by volume, and lines of oil were placed across the span upstream of the model and on the compression surface of the model. The oil was fluoresced using an ultraviolet LED light bar, and images were recorded at 4K resolution and 120 Hz using a GoPro HERO9 camera suspended above the tunnel with a 575 nm longpass filter and viewing the floor of the test section in addition to the top surfaces of the model. Between the times of the tunnel startup and unstart (during steady state conditions), the oil flow outlined constant average streaklines along the floor and did not vary through the run. The images clearly distinguished where the quasi-conical or quasi-cylindrical symmetry between the separation and reattachment lines was fully developed, thus aiding in the placement of the stereoscopic PIV plane in the *x-y* dimension (streamwise-wall normal). The oil flow results were also used to compare with the stereoscopic particle image velocimetry results in order to find a threshold velocity value for the beginning of the separated region near the floor.

3.4 Particle Image Velocimetry Setup

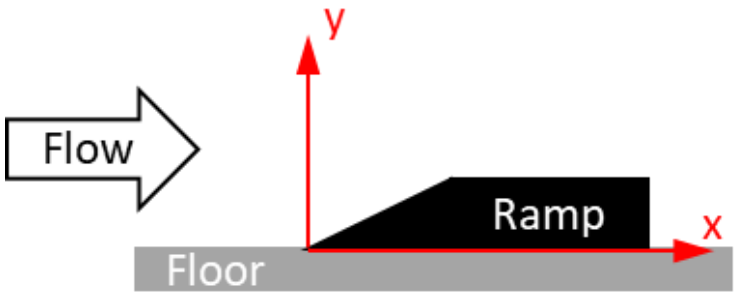
Particle image velocimetry (PIV) was used to record instantaneous velocity vector fields near and around the separation region. The planar PIV experiments were designed to measure subsonic velocities in a large spanwise area leading up to the compression ramp, whereas the stereoscopic PIV experiments were designed to measure a streamwise floor-normal vector field along the centerline of the model. The stereoscopic results can be used to reference and validate the

Distribution is unlimited/AFRL-2023-2280; Cleared 05/11/2023



a)





b)

Figure 3.3. Schematic of the oil flow visualization experiment from a (a) top-down perspective and (b) side perspective. The orange lines are where the oil flow is applied before a run begins.

Distribution is unlimited/AFRL-2023-2280; Cleared 05/11/2023

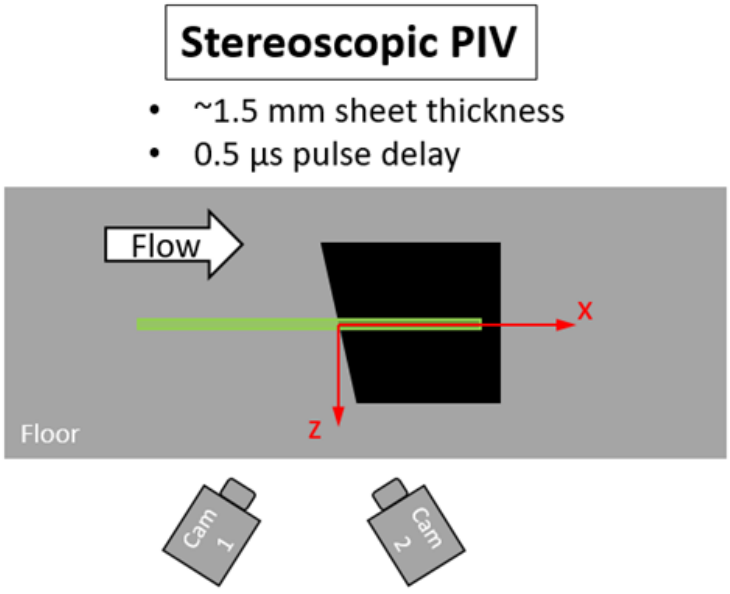
planar results through varying heights in the boundary layer. Due to their highly reflective properties and ease of cleaning off of surfaces, Aeroxide P25 Titanium(IV) Dioxide (TiO_2) particles from Acros Organics were seeded into the flow upstream of the nozzle using a fluidized bed. The fluidized bed was pressurized above 32 psi in order to be greater than the stagnation pressure of 30.5 psi in the stilling chamber allowing the particles to enter the chamber. In PIV, the Stokes number is a dimensionless number that is used to determine the capability of a particle to follow the flow inside the flow of a fluid. For flow conditions inside this wind tunnel, titanium dioxide particles were calculated in Kocher [40] to have a Stokes number of 0.1 which is found to be low enough (below a value of 0.2) for the particles to accurately follow the flow.

3.4.1 Streamwise-Wall Normal (x-y) Plane Stereoscopic PIV

Stereoscopic PIV (2 dimensions – 3 components) was conducted at a 30 Hz acquisition rate using two LaVision Imager CX-12 cameras focused on the same field in the laser sheet using scheimpflug adaptors, 55 mm Nikon camera lenses, and 532 nm bandpass filters. The laser used was an Evergreen HP Nd:YAG laser (532 nm) which can produce up to 300 mJ/pulse. For both PIV experiments, the lasers produced approximately 21 mJ/pulse as measured by a Coherent FieldMaxII-TOP laser power/energy meter. The region of interest was focused on the incoming boundary layer and the separation region along the centerline of the SCRs with a laser sheet approximately 1.5 mm thick in the *x-y* plane. Figure 3.4 displays both a simple diagram and a photograph of the stereo PIV setup. The image pairs were captured with a Δt of 0.5 µs to give a freestream particle displacement of ~13 pixels. LaVision's DaVis v10.2 software suite was used to acquire images and process the vector fields from image pairs. With an image resolution of 3995 x 1733 pixels, a total field of 333 x 145 vectors was

Distribution is unlimited/AFRL-2023-2280; Cleared 05/11/2023

a)



b)

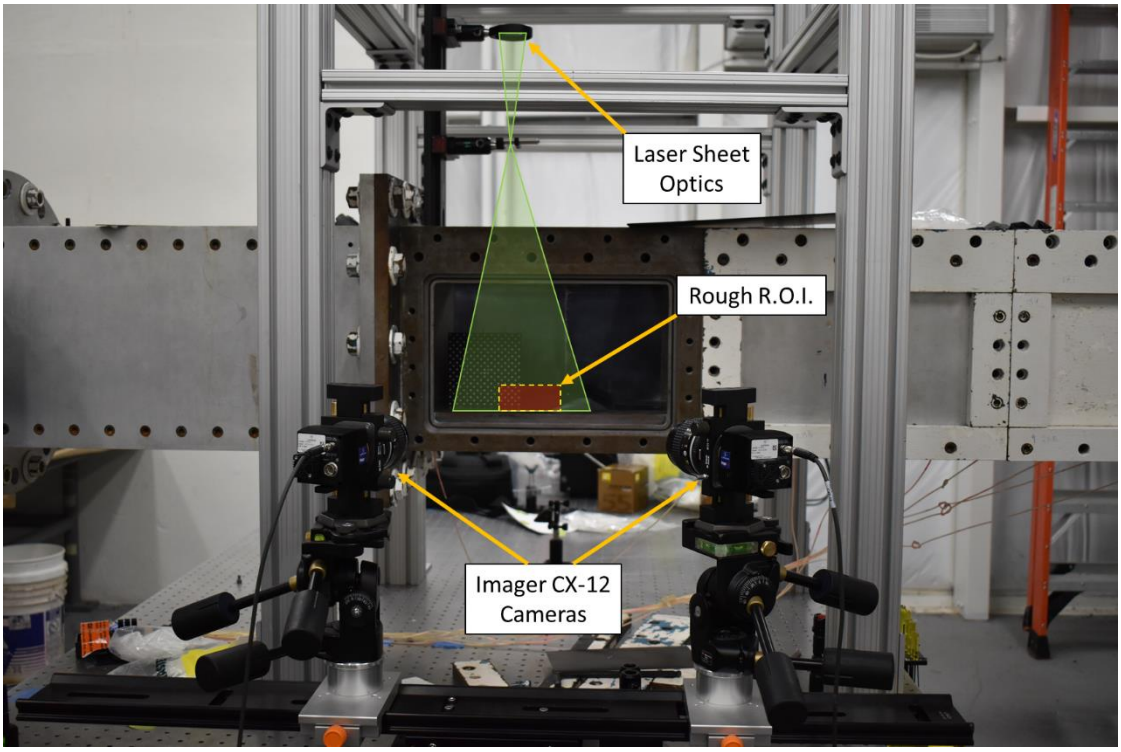


Figure 3.4. a) Diagram of the configuration for stereo PIV. b) Photo of experimental setup for stereo PIV.

Distribution is unlimited/AFRL-2023-2280; Cleared 05/11/2023

computed per image-pair for both sweep models with a distance of 0.98 mm between adjacent vectors.

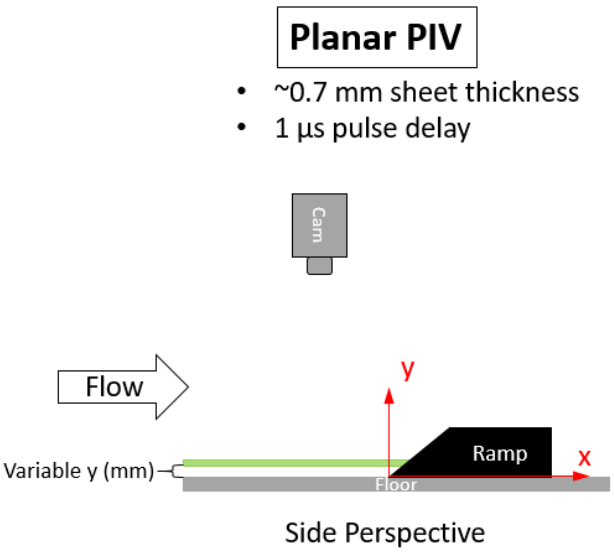
3.4.2 Streamwise-Spanwise (x-z) Planar PIV

Planar PIV was conducted at 30 Hz using the same equipment as the stereoscopic PIV experiments. However, only one of the CX-12 cameras was used with a Δt of 1 µs between image pairs with a particle displacement of ~14 pixels for each case, and the laser sheet, with a thickness of about 0.7 mm, was in the *x-z* plane at variable heights in the boundary layer of 2 mm, 4.5 mm, and 8 mm off the floor of the test section. Figure 3.5 displays both a simple diagram and a photograph of the planar PIV setup. With an image resolution of 2752 x 1552 pixels and a distance of 1.57 mm between each vector, the vector field size for the y = 2 mm case had a total field size of 230 x 130 vectors computed per image pair for the 30° sweep and a total field of 187 x 130 vectors for the 10° sweep. For y = 4.5 mm and an image resolution of 2496 x 1552 with 1.55 mm between each vector, the 30° sweep had a total field of 230 x 130 vectors while the 10° sweep had a total field of 208 x 130 vectors. For y = 8 mm and an image resolution of 2854 x 1552 with 1.56 mm between each vector, the 30° sweep had a total field of 246 x 130 vectors while the 10° sweep had a total field of 224 x 130 vectors. The vector field resolution was smaller in the 10° case relative to the 30° case due to less sweep requiring a smaller region of interest.

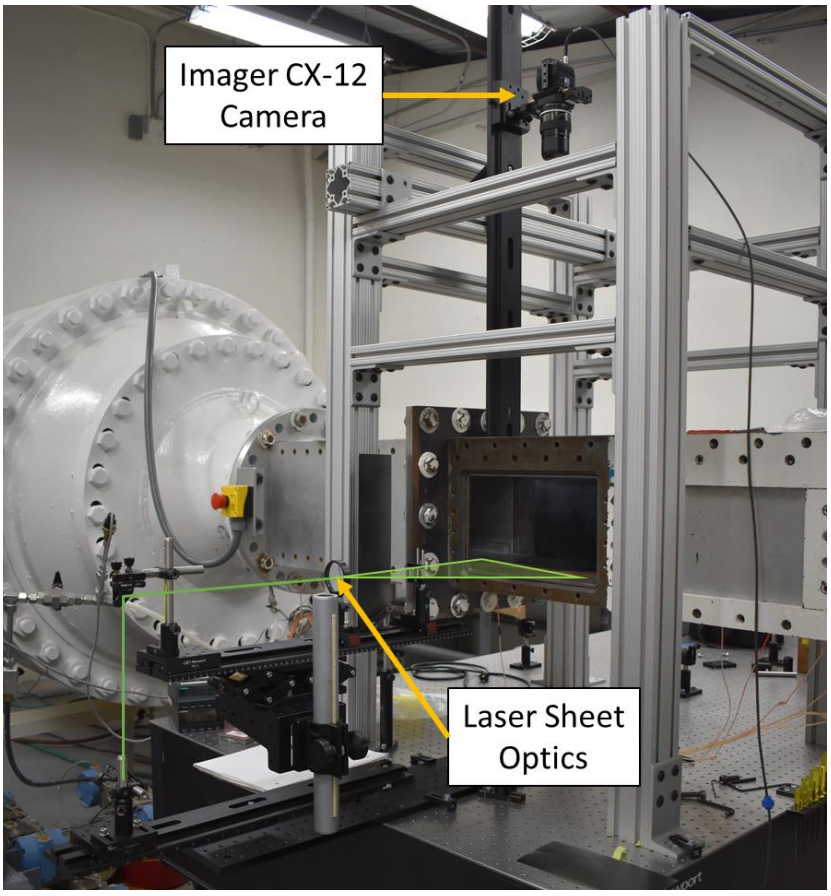
3.4.3 PIV Data Processing Procedures

Vector calculations were done with the multi-pass algorithm in DaVis v10.2. The first interrogation window was four passes with an elliptical weight of 2:1 (in the streamwise direction) for a 128 x 128 pixel region with 50% overlap, followed by eight passes of an adaptive interrogation window with a size of 48 x 48 pixels with 75% overlap. Post-processing used a universal outlier detection scheme with

Distribution is unlimited/AFRL-2023-2280; Cleared 05/11/2023



a)



b)

Figure 3.5. a) Diagram of the configuration for planar PIV. b) Photo of experimental setup for planar PIV.

Distribution is unlimited/AFRL-2023-2280; Cleared 05/11/2023

three passes over a region of 5 x 5 vectors in order to remove erroneous vectors. Vector fields were removed during further post-processing in MATLAB R2021a if they fell under one of two parameters: if more than 5% of the total vectors were missing from the sequence, or if more than 5% were outside of two standard deviations from the mean value. After removing the erroneous vector fields, they were ensemble-averaged again over each vector component and then the velocity magnitude over each component of the vector fields was taken after this process. When choosing the pixel regions for the interrogation windows, this investigation aimed for a typical PIV [41] seeding density of 10 particles per vector and a maximum displacement of 20 pixels recorded.

3.5 Unsteady Pressure Sensitive Paint Anchored with 4 Pressure Transducers

3.5.1 Experiment Details

These experiments show unsteady PSP with a frequency response up to 20 kHz on the SCR models providing global surface pressure measurements from an effective range of 0.14 psi to 29 psi, and it was run in tandem with 2 Kulite XTEL-190L-25A Pressure Transducers, able to record pressures up to 25 psi, and a Kulite KSC-2 High Performance Signal Conditioner recording at 40 kHz leading up to the model along the centerline. Due to size restrictions, only two transducers were used during a single run, so these experiments were split into two cases for each sweep angle. Case 1 had pressure taps located at positions $3.5\delta_{99}$ and $1.5\delta_{99}$ upstream of the ramp edge along its centerline, while case 2 had pressure taps located at positions $3\delta_{99}$ and $0.5\delta_{99}$. These locations were chosen to be able to investigate multiple points in the separation region and to anchor the PSP results. The PSP was applied over an area of the full span of both models, the entire ramp surface, and upstream of the centerline of $8.7\delta_{99}$ for the 10° sweep model and $6.9\delta_{99}$ of the 30° sweep model. Figure 3.6 shows the configuration for this

Distribution is unlimited/AFRL-2023-2280; Cleared 05/11/2023

experiment. A Photron FASTCAM Mini AX-200 camera, with a 575 nm longpass filter, recorded the PSP data at 20 kHz using Photron FASTCAM Viewer v4. Two water-cooled, continuous ultraviolet LEDs from Innovative Scientific Solutions, Incorporated (ISSI) capable of producing a 400 nm wavelength light with a power output rating of ~ 13 W were utilized for this experiment. The camera, LEDs, and pressure transducers were timed using a Berkeley Nucleonics Model 577 Pulse Generator. The point-of-view of the camera was aimed at the tunnel floor, similar to the experimental setup for the planar PIV experiment.

3.5.2 Pressure Transducer Data Processing Procedures

The two pressure transducers used in this experiment were calibrated through the use of a Druck DPI 612 Pressure Calibrator with a PM620, 2 bar absolute, Pressure Module before the experiments were run. Using the calibrated values for each transducer, the data recorded from the experiments were then converted from units of mV to psia in Microsoft Excel and placed into MATLAB R2021a and converted into a power spectral density using the pwelch command with the inputs: a Hanning window, 75% overlap, with a number of 2048 discrete Fourier transform points, and a sampling frequency of 40 kHz. A power spectral density (or PSD) was then computed for P' using the pwelch command with the inputs: a Hanning window, 75% overlap, 2048 discrete Fourier transforms, and a sampling frequency of 40 kHz. Results were multiplied by the output frequency and normalized by their respective variance.

3.5.3 PSP Data Processing Procedures

For PSP, every pixel is essentially treated as a pressure transducer. Across the entire measurement region, each high sweep image featured a data density of 187845 pixels, and each low sweep image featured a data density of 243332

Distribution is unlimited/AFRL-2023-2280; Cleared 05/11/2023

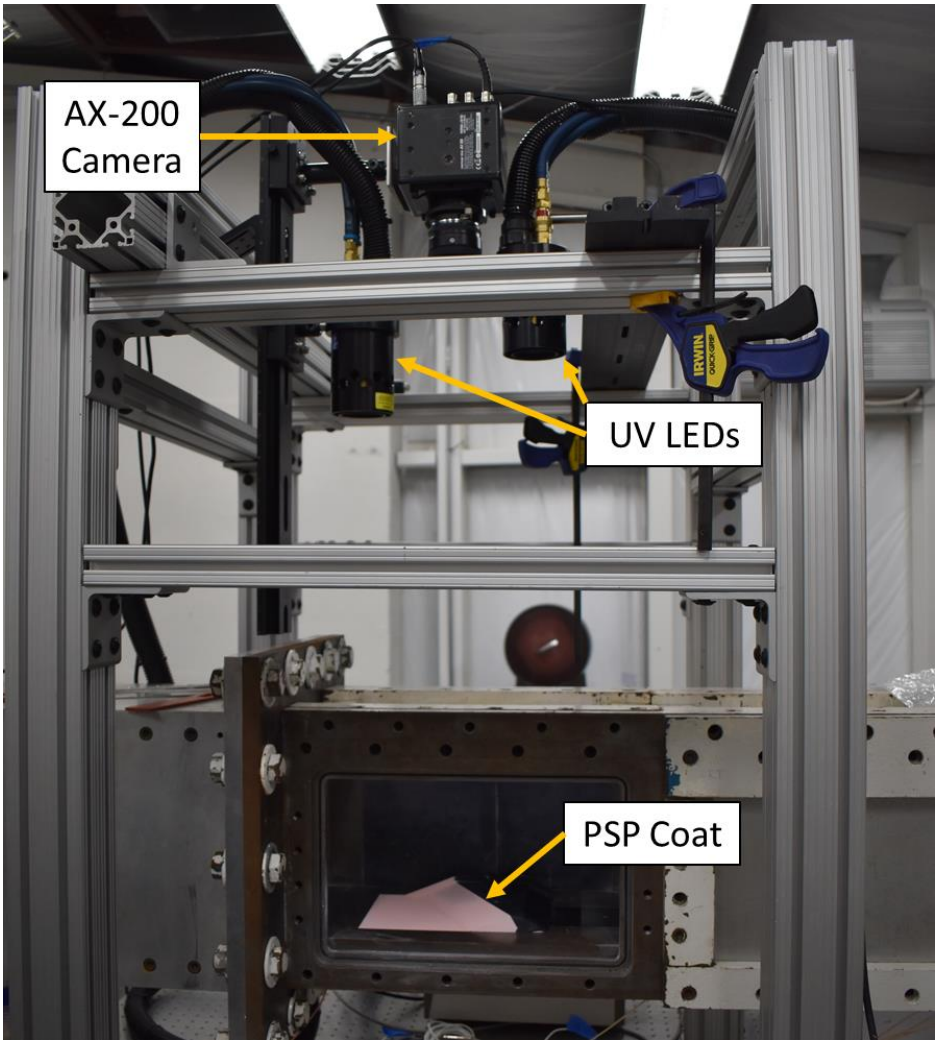


Figure 3.6. Photo of uPSP experimental setup with PSP coat applied onto 30° λ_{sweep} model.

Distribution is unlimited/AFRL-2023-2280; Cleared 05/11/2023

pixels. The images were transferred from PFV4 to MATLAB and processed using an inhouse code explained in this paragraph. The intensity ratios were found by dividing 2000 wind-on frames from 1000 wind-off frames. Calibration curves provided by ISSI were used to create the resulting pressure fields. Using the imgaussfilt command, a 2D Gaussian smoothing filter with a 0.75 standard deviation was placed over each instantaneous pressure field to reduce the amount of erroneous individual pixels. An ensemble averaged image and a standard deviation image was taken from the set of 2000 frames. The mean pressure field was subtracted from the instantaneous pressure fields to find the instantaneous pressure fluctuations *P'*. A PSD was then computed for *P'* using the pwelch command with the inputs: a Hanning window, 75% overlap, 500 discrete Fourier transforms, and a sampling frequency of 20 kHz. The PSDs were then multiplied by their respective output frequency vector, divided by their respective variance, and subsequently shown in graphs.

3.6 Uncertainty Discussion

3.6.1 Particle Image Velocimetry

The quantifiable uncertainty of the PIV results was estimated in an *a-posteriori* method using a generic post-processing technique in DaVis using a statistical analysis of the correlation process between the patterns of intensity among an image-pair fully explained by Wieneke [42]. The post-processing technique was further investigated which found the uncertainty estimation to be reasonably accurate [43-45]. The uncertainty results are discussed later in section 4.2.3.

Physical sources of uncertainty mentioned hereafter were present in these experiments that were unable to be quantified in these results. The seed particles were not baked in an oven to ensure there was no clumping of the particles. These experiments were taken on humid summer days in Tennessee, so the glass

Distribution is unlimited/AFRL-2023-2280; Cleared 05/11/2023

windows tended to fog up during some runs. These runs were not processed in the final results if the fog was noticeable to the human eye in the raw images, but some blurring could have still occurred to a point in which DaVis was unable to process the full vector fields accurately in every run. Even after spray-painting the models dark black and using a Sharpie to draw the floor black, the laser glare and reflections over the surface of the ramp and at some parts of the floor created some noticeable artifacts in the results. For the technique to discover the separation threshold using the oil flow and stereoscopic PIV results, the laser glare prevented the ability to find a separation threshold very close to the floor (within half a millimeter), thus the threshold was measured within 1 mm to the floor which could provide some uncertainty in finding the actual shock foot position.

3.6.2 Unsteady Pressure Sensitive Paint

The uPSP diagnostic technique has inherent uncertainties with applying the coats of paint as it can be more of an art than a science. The response of the paint is affected by the roughness of the surface of the coat, thickness of the layer of paint, application method of the coat, the formula of PSP used, and the underlying material that the paint is applied on to. The effect of different underlying materials is shown in the PSP results in section 4.3. The humidity of the humid summer Tennessee days also affected the base coat of the paint which resulted in some of the paint chipping off of the 30° swept ramp. However, in regards to error, this research focuses on quantifying the systematic error of the pressure recorded in the PSP images with respect to the data recorded by the pressure transducers. This was done by calculating the difference between the mean value recorded at each pressure transducer relative to the pressure recorded in the ensemble-averaged PSP images at a location directly above and below each pressure transducer. The 30° sweep images had, on average, an absolute error of ± 0.15 psi, and the 10° sweep images had an average absolute error of ± 0.68 psi. The higher error for the lower swept case could be attributed to needing to conserve

Distribution is unlimited/AFRL-2023-2280; Cleared 05/11/2023

the expensive top coat for other time-sensitive experiments outside of the scope of this study by using half of the amount of topcoat as was used in the higher swept case.

The combined non-linearity, hysteresis, and repeatability error reported by Kulite for these pressure transducers are ± 0.1% of 100 mV which results in an uncertainty of ~ ± 0.027 psi. Druck reports the pressure calibrator and pressure module are each accurate from 0.005% of the full-scale operating range which equates to an uncertainty of ~ ± 0.0015 psi for both the calibrator and pressure module.

Distribution is unlimited/AFRL-2023-2280; Cleared 05/11/2023

CHAPTER 4
EXPERIMENTAL RESULTS

4.1 Oil Flow Visualization

In Figures 4.1 and 4.2, fluorescent oil flow shows the streaklines of the flow over the surface of the wind tunnel floor and models along with a distinct difference in the fully developed symmetry of the separation and reattachment lines between the high and low sweep cases. As seen in Figure 4.1, the 10° sweep case has a quasi-cylindrical symmetry denoted where the separation and reattachment lines are approximately parallel, and thus the streamwise extent of the separation region appears to remain constant along the span of the model. The inception region, where the symmetry is not yet fully developed near the apex of the leading edge, seems to experience a recirculation vortex of the 10° model. The cause of this could be some sort of relief effect due to the most upstream portion of the resin-printed fence not being flush with the floor of the test section. This seemed to be allowing the buildup of flow to escape under the fence, which may have affected the spanwise length of the inception region. Although since the further results of every experimental case are recorded in the fully developed symmetry regions, this should not provide any significant error in this thesis. In Figure 4.2, the 30° sweep case features a quasi-conical symmetry where the separation region grows along the span as the fluid travels further along the sweep due to significant crossflow causing the separation line and the reattachment line to diverge from the compression corner of the ramp. The virtual conical origin was also traced back from the fully developed symmetric lines.

Oil flow over the 30° sweep showed an average separation location to be $x_{sep} \sim 1.9\delta_{99}$ upstream of the compression corner along the centerline. Oil flow over the 10° sweep showed an average separation location to be $x_{sep} \sim 1.4\delta_{99}$ from the compression corner along the centerline, which resulted in $\Delta x_{sep} \sim 0.5\delta_{99}$ between

Distribution is unlimited/AFRL-2023-2280; Cleared 05/11/2023

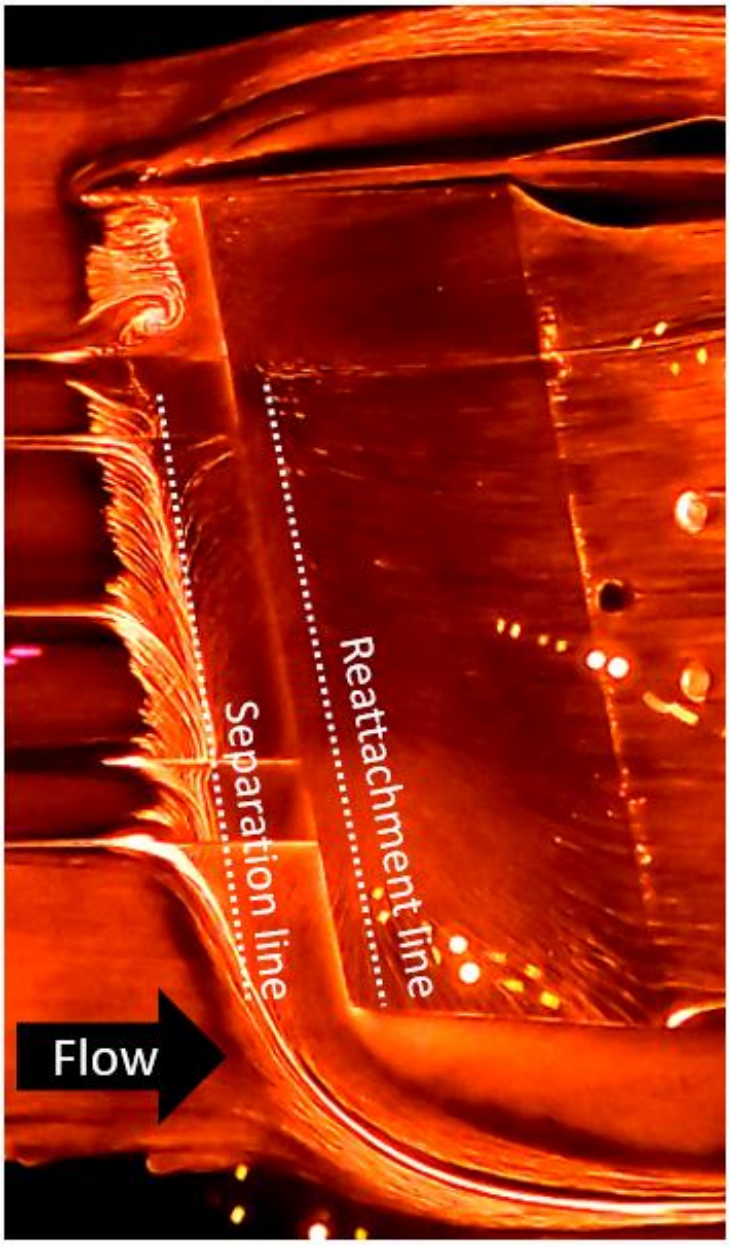


Figure 4.1. Fluorescent oil flow showing quasi-cylindrical symmetry between the boundary layer separation line and reattachment line of the boundary layer around the separation region of the 10° λ_{sweep} compression ramp.

Distribution is unlimited/AFRL-2023-2280; Cleared 05/11/2023

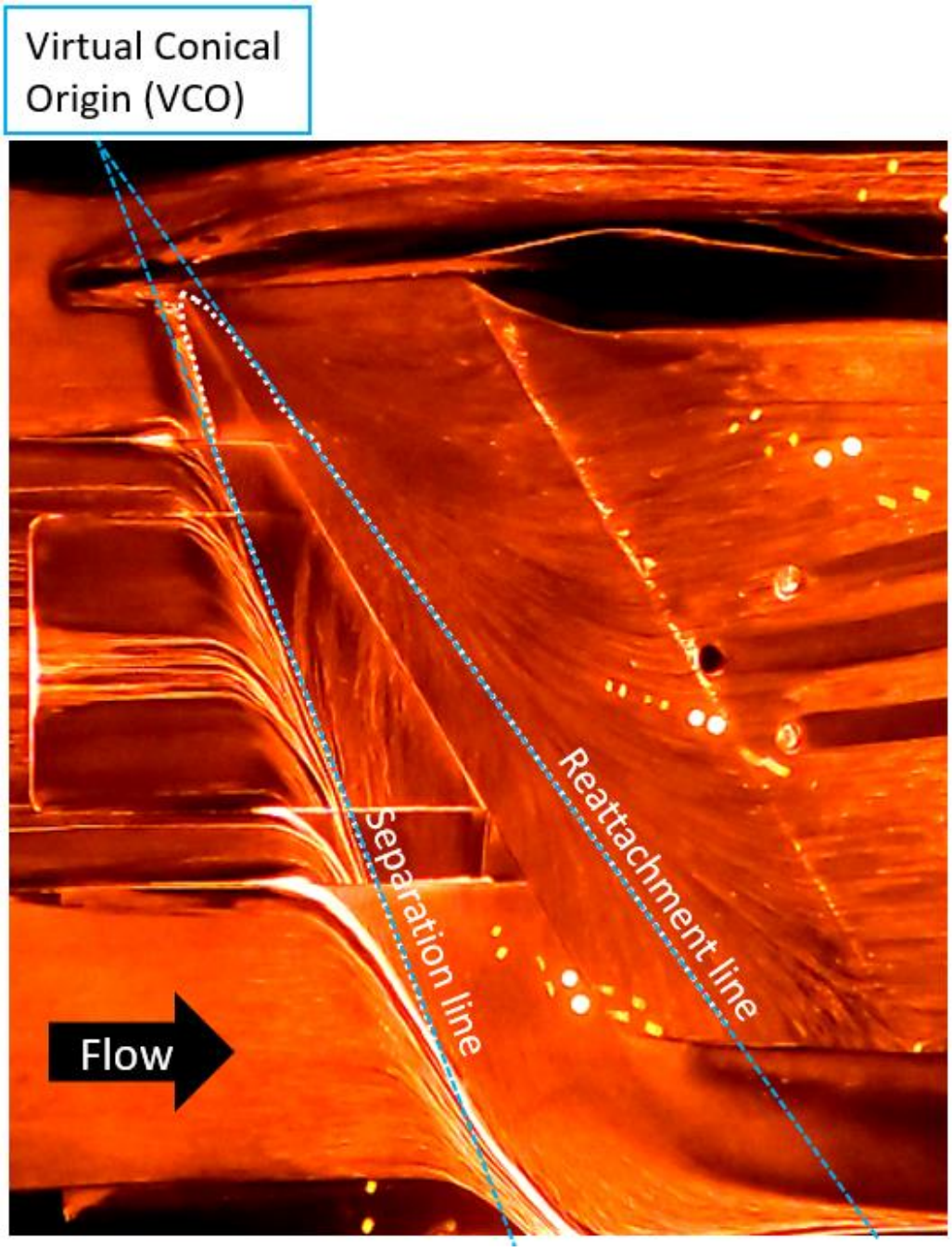


Figure 4.2. Fluorescent oil flow showing quasi-conical symmetry between the boundary layer separation line and reattachment line of the boundary layer around the separation region of the 30° λ_{sweep} compression ramp.

Distribution is unlimited/AFRL-2023-2280; Cleared 05/11/2023

the two ramps. The inviscid shock strength for the low sweep case is higher at a value of P_2/P_1 = 3.26 for the 10° sweep than the higher sweep case at a value of P_2/P_1 = 2.48. The higher shock strength of the low sweep case would denote a larger separation region; however, the high sweep case has a quasi-conical symmetry which means the separation region increased in size as it traveled down the span of the model. By the centerline of the model, the size of the separation region depends more on the distance from the virtual conical origin rather than the strength of the shock.

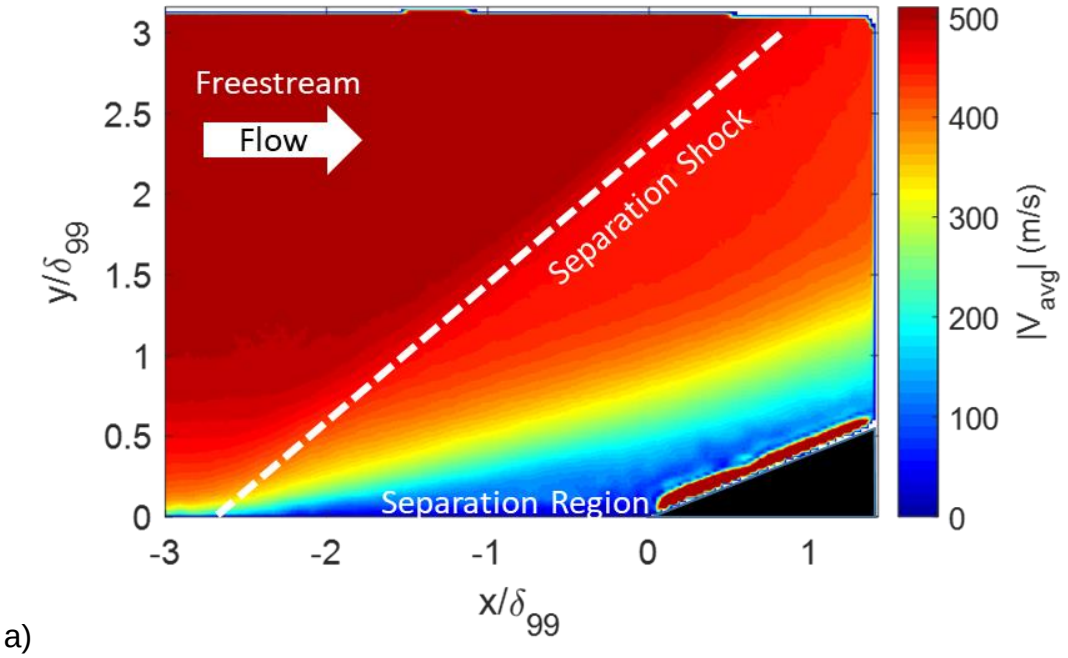
4.2 Stereoscopic and Planar PIV Results

The results for stereoscopic PIV are reported first to show how the separation point was recorded for the planar PIV results. The vector fields recorded in DaVis and postprocessed in MATLAB were used to identify subsonic velocities and the first streamwise location that the minimum velocity threshold for separation was reached near the floor.

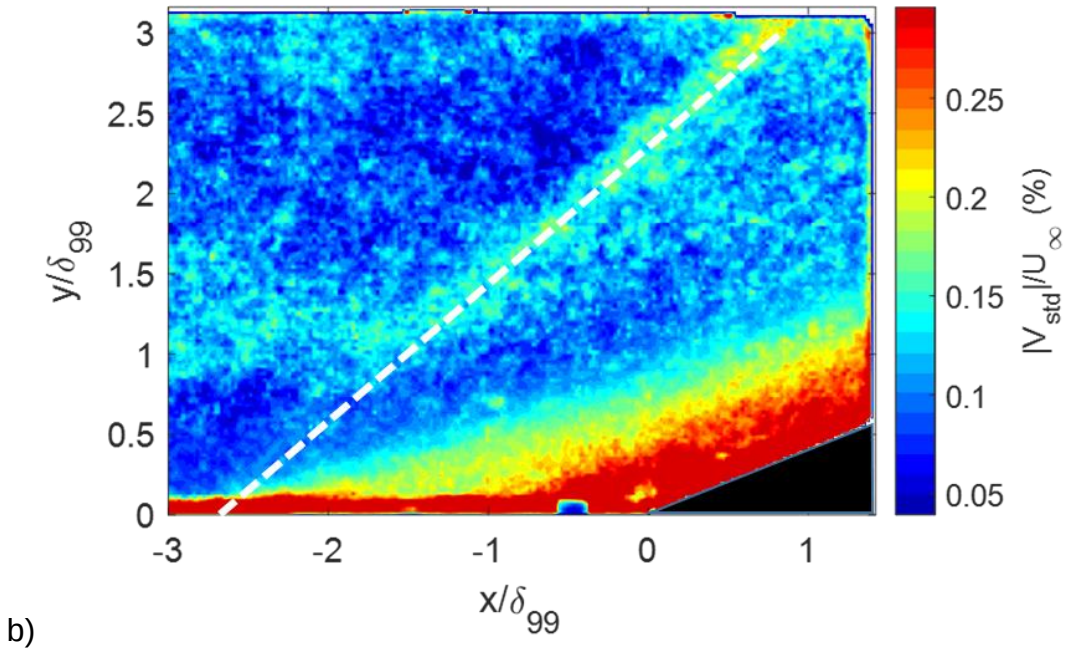
4.2.1 Stereoscopic PIV

Ensemble-averaged and standard deviation vector fields were calculated over multiple tunnel runs for both sweep cases and are shown in Figure 4.3 over 1361 image-pairs for the 30° swept ramp and in Figure 4.4 over 722 image-pairs for the 10° swept ramp. Here, the magnitudes of the velocities are shown in the contours as opposed to either component of velocity being shown independently to view the subsonic velocities as Mach number is determined using the magnitude of all the spatial vector components of the flow. The turbulent boundary layer velocity profile at x/δ_{99} = -3 was recorded from the resulting averaged streamwise velocity vector, U_{avg}, in Figure 4.5 (a) for the high sweep and Figure 4.6 (a) for the low sweep. The turbulent profiles were then transformed into the inner scales using

Distribution is unlimited/AFRL-2023-2280; Cleared 05/11/2023



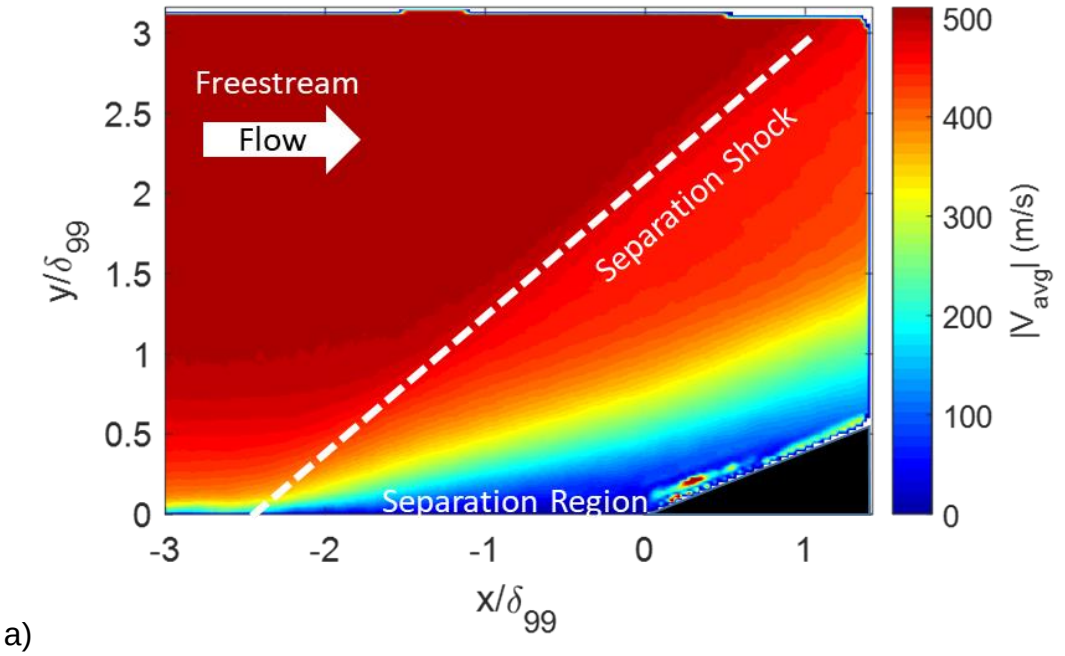
a)



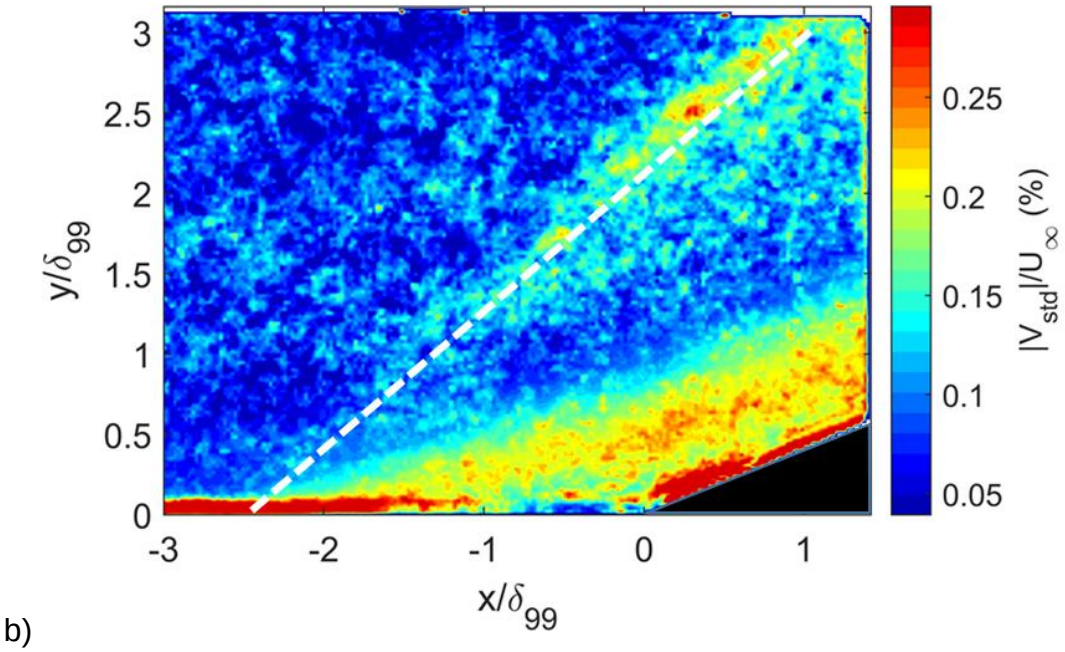
b)

Figure 4.3. Stereoscopic PIV results for 30° λ_{sweep} showing (a) the ensemble-averaged velocity magnitude and (b) the standard deviation of the velocity magnitude.

Distribution is unlimited/AFRL-2023-2280; Cleared 05/11/2023



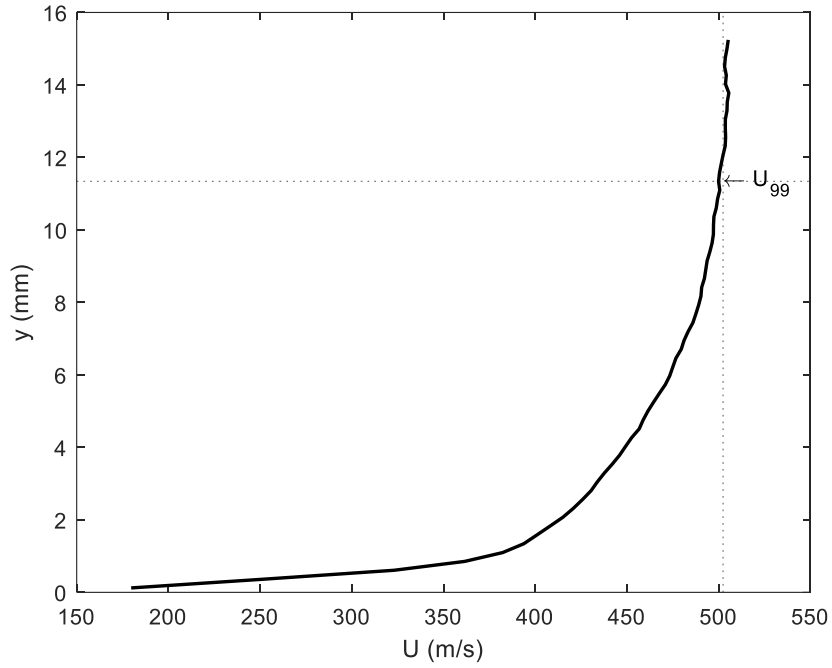
a)



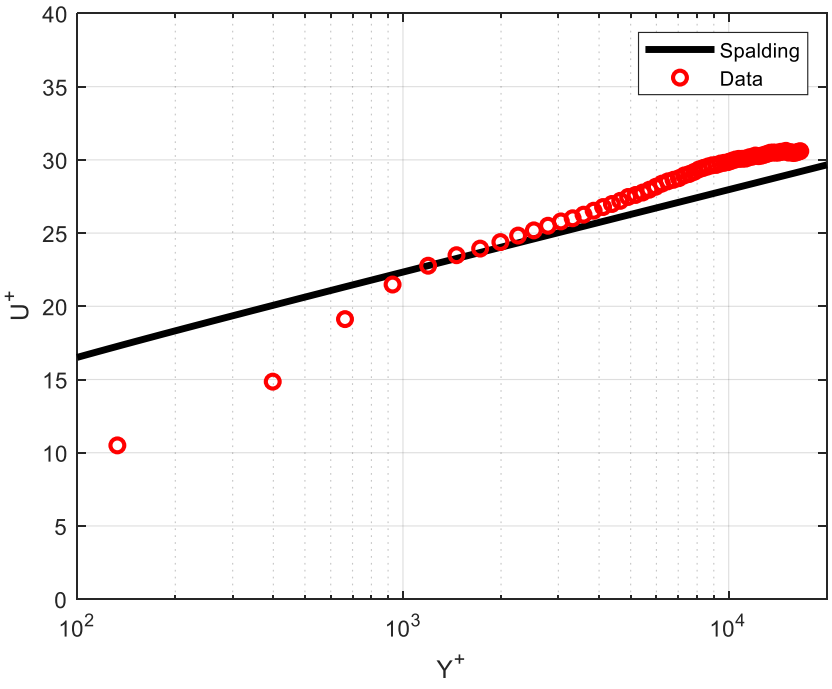
b)

Figure 4.4. Stereoscopic PIV results for 10° λ_{sweep} showing (a) the ensemble-averaged velocity magnitude and (b) the standard deviation of the velocity magnitude.

Distribution is unlimited/AFRL-2023-2280; Cleared 05/11/2023



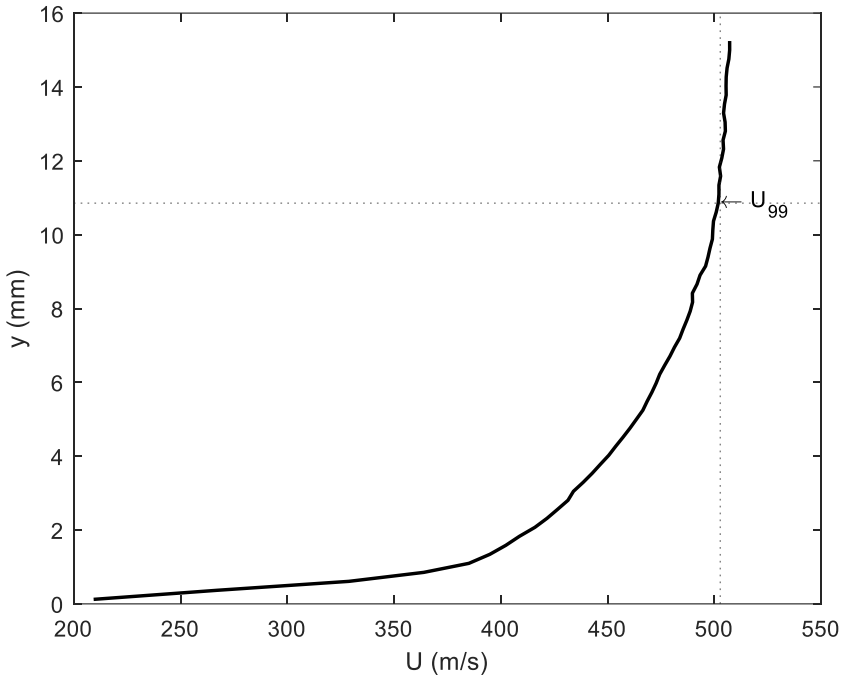
a)



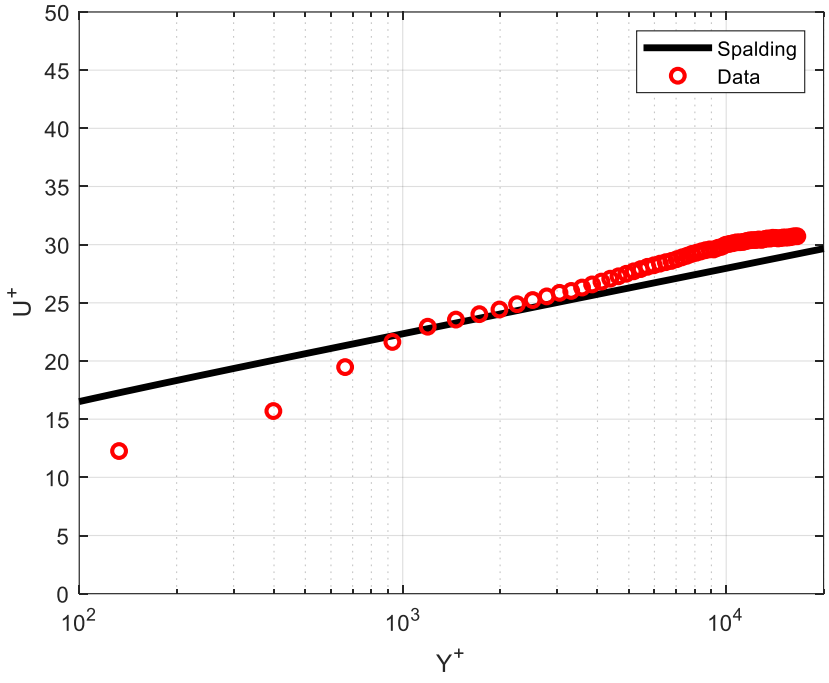
b)

Figure 4.5. a) Turbulent boundary layer velocity profile and b) Van-Driest velocity transform at x/δ_{99} = -3 for the 30° λ_{sweep} case.

Distribution is unlimited/AFRL-2023-2280; Cleared 05/11/2023



a)



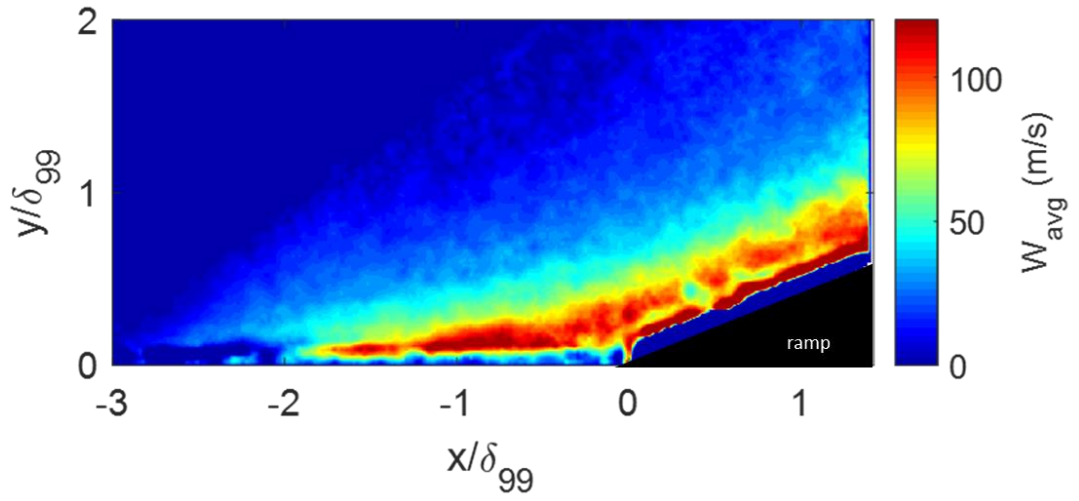
b)

Figure 4.6. a) Turbulent boundary layer velocity profile and b) Van-Driest velocity transform at x/δ_{99} = -3 for the 10° λ_{sweep} case.

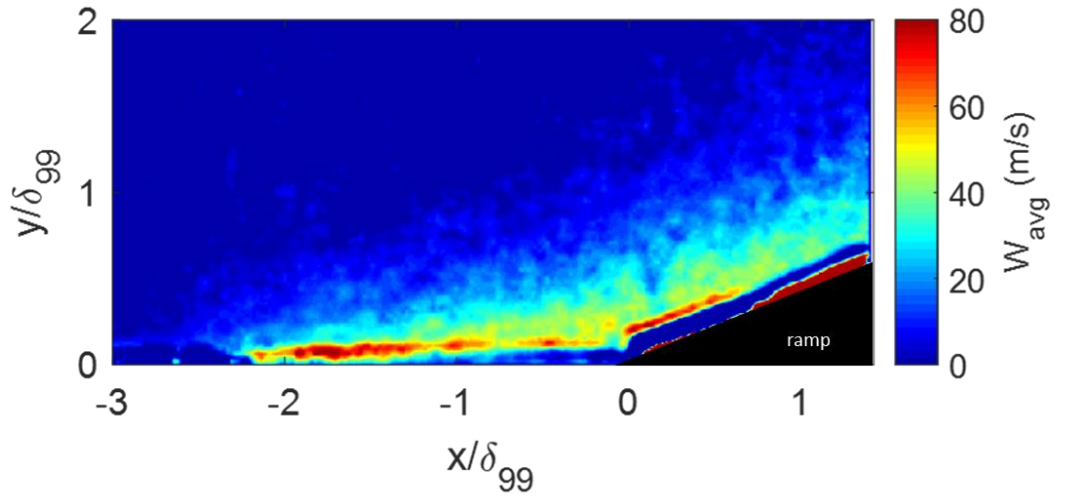
Distribution is unlimited/AFRL-2023-2280; Cleared 05/11/2023

the Van-Driest transform, which validates the accuracy of these profiles with nondimensionalized turbulent profiles found in literature, in Figure 4.5 (b) for the high sweep and Figure 4.6 (b) for the low sweep. The U_{99} value shown in Figures 4.5 (a) and 4.6 (a) calculated from the average streamwise velocity in the freestream at $x/\delta_{99} = -3$ is close to the $\delta_{99} = 11$ mm height reported by Kocher [40] for both cases with a δ_{99} of ~11.2 mm for the 30° sweep and ~10.9 mm for the 10° sweep. The average crossflow velocity, W_{avg}, fields can be seen in Figure 4.7 (a) for the 30° sweep case and Figure 4.7 (b) for the 10° sweep case. The compression ramp starts at $x/\delta_{99} = 0$ along the x-axis of the figures. The freestream, separation region, and separation shock can be easily inferred from the two images and are also annotated on the figures for clarity. The freestream is characterized as the region with high average velocity values near the expected nominal velocity of 507 m/s and a low standard deviation of the velocity meaning it does not change significantly from those average values. The subsonic region is characterized by the large region wherein the velocity magnitudes are less than 255 m/s. The ensemble-averaged separation location can be inferred by noting where the average freestream velocities suddenly decrease and their standard deviation suddenly increases. This sudden change is indicative of the separation shockwave which is easily visible upon initial inspection. In Figure 4.3, the intersection of this shock with the tunnel floor determines $x_{sep} \sim -2.7\delta_{99}$ mm on the x-axis. Vanstone, et al. [24] report an average separation location of $2\delta_{99}$ for a 30° swept ramp, with the same compression angle of 22.5° and Mach number of 2. The discrepancies between the current findings and those reported by Vanstone, et al. [27] are to be expected as the present experiment has a larger spanwise extent and both measurements were made along the centerline of the models. Considering the oil flow visualization results reported in Vanstone, et al. [28], there is good agreement between measurements made at similar locations. It is important to note that the effect of laser glare near the surface of the compression

Distribution is unlimited/AFRL-2023-2280; Cleared 05/11/2023



a)



b)

Figure 4.7. Stereoscopic PIV results for the ensemble-averaged crossflow velocity field for (a) the 30° λ_{sweep} and (b) the 10° λ_{sweep}.

Distribution is unlimited/AFRL-2023-2280; Cleared 05/11/2023

ramp oversaturated the raw images which resulted in an erroneous region of ~ 0.9 mm normal to the surface of the ramp.

Similar methodologies were applied to the 10° sweep case, and the results shown in Figure 4.4 reveal that x_{sep} ~ -2.5δ_{99} mm for this case. These quantitative results agree with the oil flow results in that the average separation region is larger along the centerline of the models for the 30° swept case than for the 10° swept case. Stereoscopic PIV shows a difference of Δx_{sep} ~ 0.2δ_{99} mm in the average separation locations between the two cases, which is slightly smaller than the difference measured via oil flow.

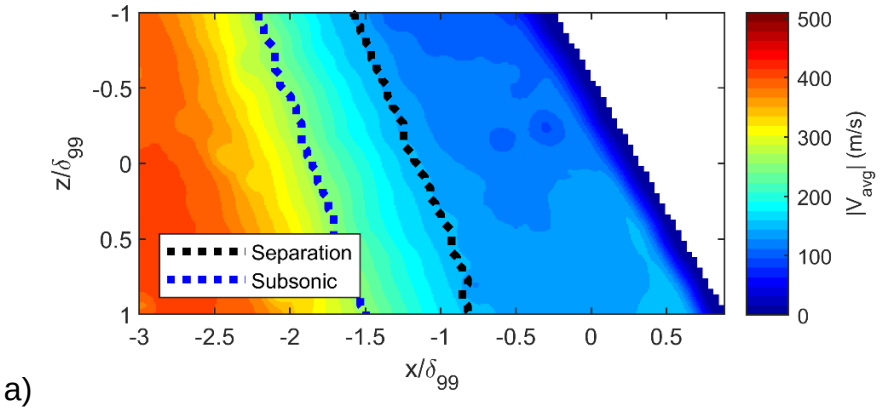
In Figure 4.7, the W_{avg} values near the floor reached up to 130 m/s for the higher swept case and 65 m/s for the lower swept case, which approximately doubled the max average crossflow near the floor when increasing the sweepback angle from 10° to 30°.

The threshold velocity for the separation location used in the y = 2 mm planar PIV results in section 4.2.2 was set at the highest average velocity at the separation location determined via oil flow and in the stereoscopic PIV results. The highest velocities observed in the separation region of the 30° sweep were ~ 130 m/s, found by comparing Figures 4.2 and 4.3 (a). The highest velocities observed in the 10° sweep separation region were ~ 110 m/s, found by comparing Figures 4.1 and 4.4 (a). The comparison process consisted of locating the average separation distance from the oil flow along the centerline and extracting the velocity in the stereoscopic PIV data for each sweep case near that point within 1 mm from the floor.

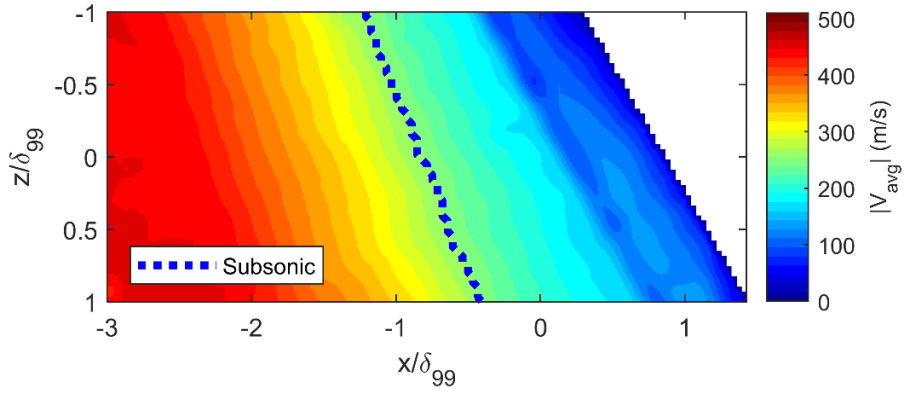
4.2.2 Planar PIV

Ensemble-averaged velocity magnitude fields from the planar PIV experiments can be seen in Figure 4.8 for the 30° sweep case and in Figure 4.9 for the 10° sweep case at each of the three heights within the boundary layer.

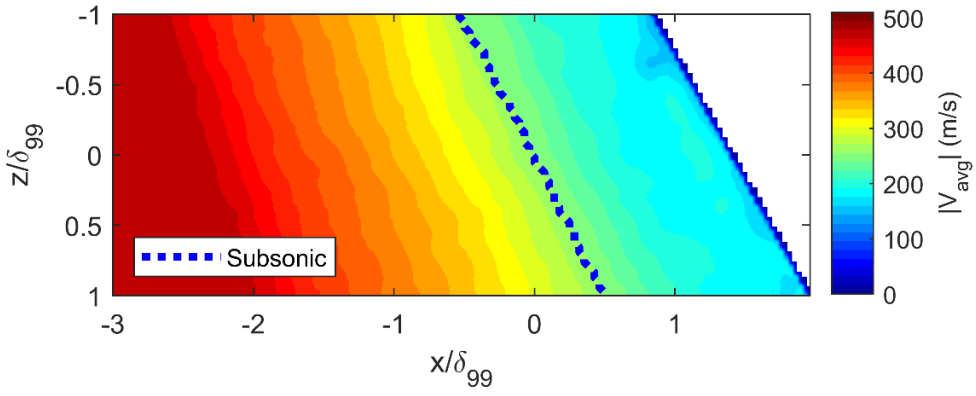
Distribution is unlimited/AFRL-2023-2280; Cleared 05/11/2023



a)



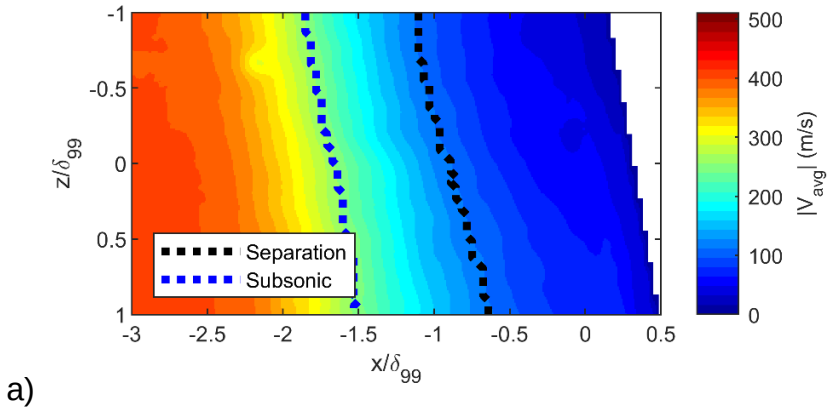
b)



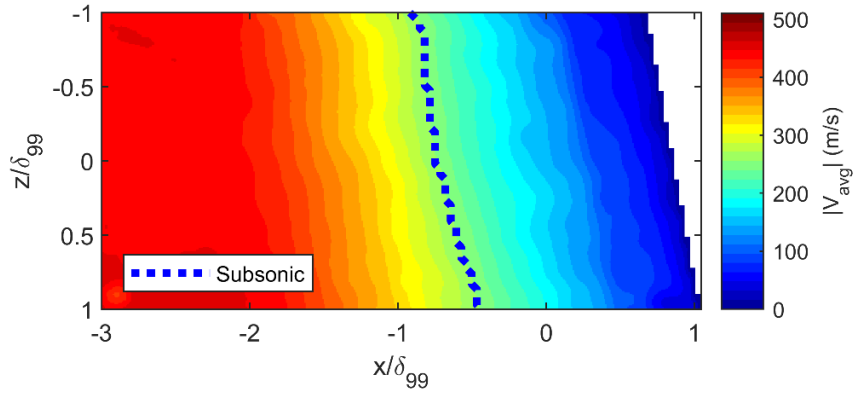
c)

Figure 4.8. 30° λ_{sweep} planar PIV, ensemble-averaged velocity magnitudes with a streamwise wall-normal laser sheet at: (a) y = 2 mm, (b) y = 4.5 mm, and (c) y = 8 mm.

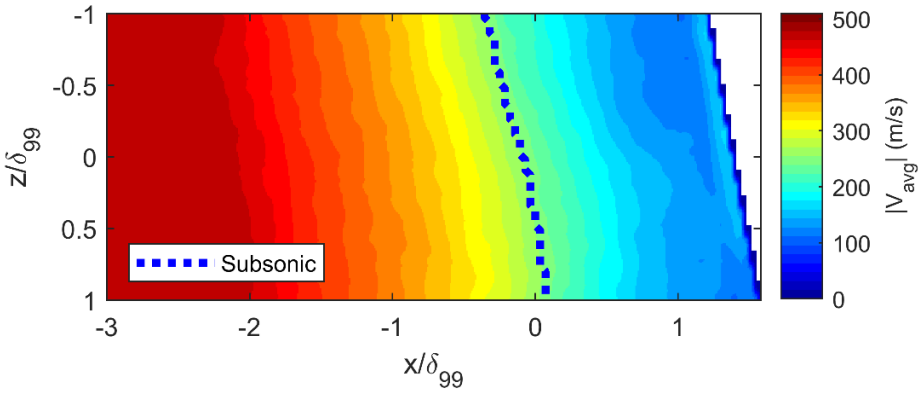
Distribution is unlimited/AFRL-2023-2280; Cleared 05/11/2023



a)



b)



c)

Figure 4.9. 10° λ_{sweep} planar PIV, ensemble-averaged velocity magnitudes with a streamwise wall-normal laser sheet at: (a) y = 2 mm, (b) y = 4.5 mm, and (c) y = 8 mm.

Distribution is unlimited/AFRL-2023-2280; Cleared 05/11/2023

Figure 4.8 (a) is at y = 2 mm and averaged over 1562 frames, Figure 4.8 (b) is at y = 4.5 mm and averaged over 1806 frames, and Figure 4.8 (c) is at y = 8 mm and averaged over 1766 frames. Figure 4.9 (a) is at y = 2 mm and averaged over 1715 frames, Figure 4.9 (b) is at y = 4.5 mm and averaged over 993 frames, and Figure 4.9 (c) is at y = 8 mm and averaged over 1370 frames. Additionally, average crossflow velocity, W_{avg}, fields can be seen in Figure 4.10 for the 30° sweep case and in Figure 4.11 for the 10° sweep case. The start of the separation region was traced only in the y = 2 mm case as this location is harder to determine higher into the boundary layer. The resulting vector fields for each boundary layer height showed areas of large standard deviations outside the range of $z/\delta_{99} > 1$ and $z/\delta_{99} < -1$. Thus, the vectors outside this region were disregarded from the subsequent analyses. By observing samples of the raw PIV particle-images, it was clear that these errors are likely due to the seeding being less consistent in those regions. The first test case conducted in this campaign was at y = 4.5 mm into the boundary layer, and the seeding seemed to be less consistent early in the experiments which possibly is the cause of the lower crossflow measurements seen comparing the y = 4.5 mm case relative to the y = 2 mm and y = 8 mm cases in Figures 4.10 and 4.11.

For the y = 2 mm planar measurements, the beginning of the separation region was located based on the velocity magnitudes. Using this separation criteria explained in section 4.2.1, the average separation location in the y = 2 mm planar case shown in Figure 4.8 (a) resulted in $x_{sep} \sim -1.15\delta_{99}$ for the centerline of the 30° swept model. In comparison to the literature where $x_{sep} \sim -1.4\delta_{99}$ at z = 0 with a planar PIV laser sheet at $y = 0.1\delta_{99}$ [28], the current result of $-1.15\delta_{99}$ with a laser sheet at $y = 0.18\delta_{99}$ seems quite reasonable, especially considering the different measurement locations within the boundary layer. Along the centerline of the 10° swept model, $x_{sep} \sim -0.89\delta_{99}$ at y = $0.18\delta_{99}$ as seen in Figure 4.9 (a). Separation was not tracked in the y = 4.5 mm and y = 8 mm cases because these planes are too far from the wall. For the higher swept case, Figure 4.10 (a) showed crossflow

Distribution is unlimited/AFRL-2023-2280; Cleared 05/11/2023

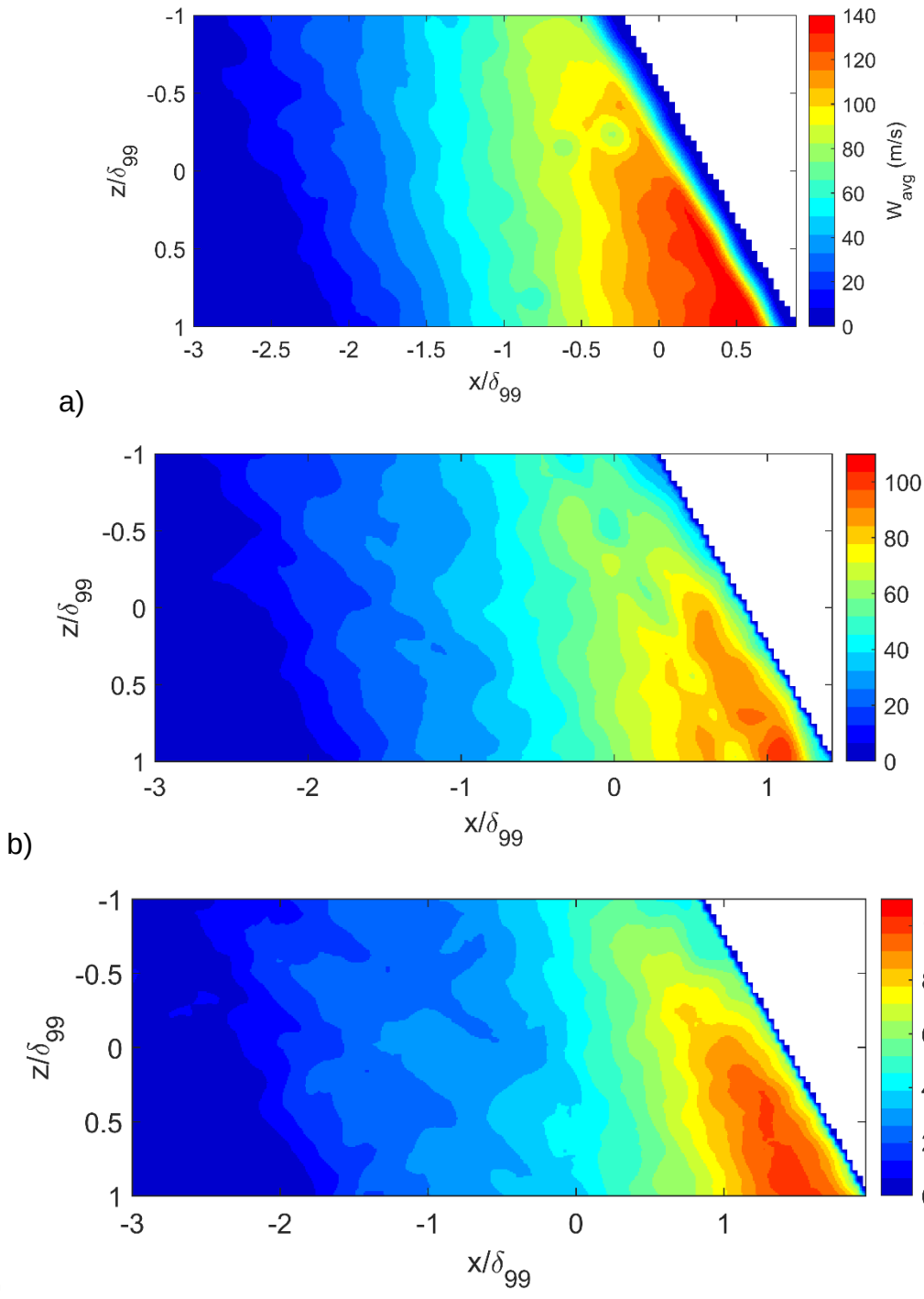
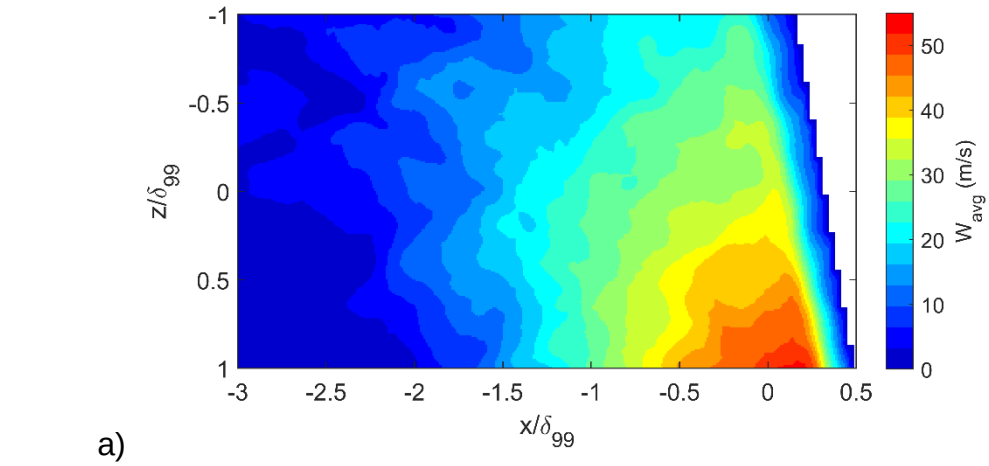
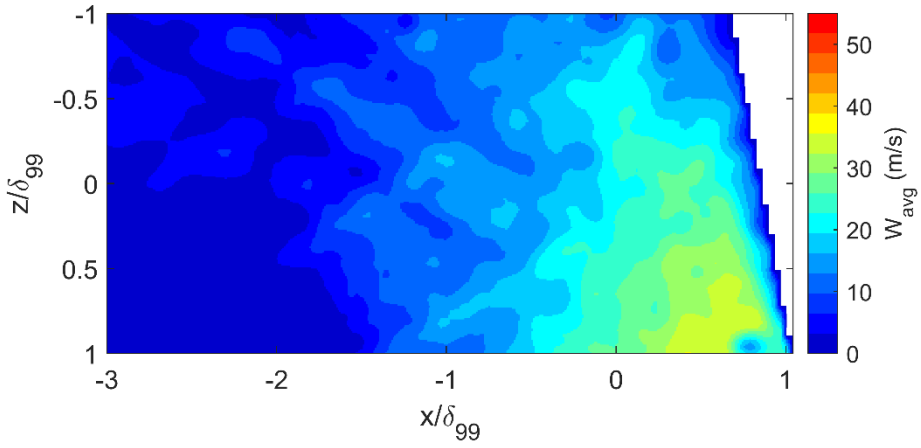


Figure 4.10. 30° λ_{sweep} planar PIV, ensemble-averaged crossflow velocity field with a streamwise wall-normal laser sheet. (a) y = 2 mm, (b) y = 4.5 mm, and (c) y = 8 mm.

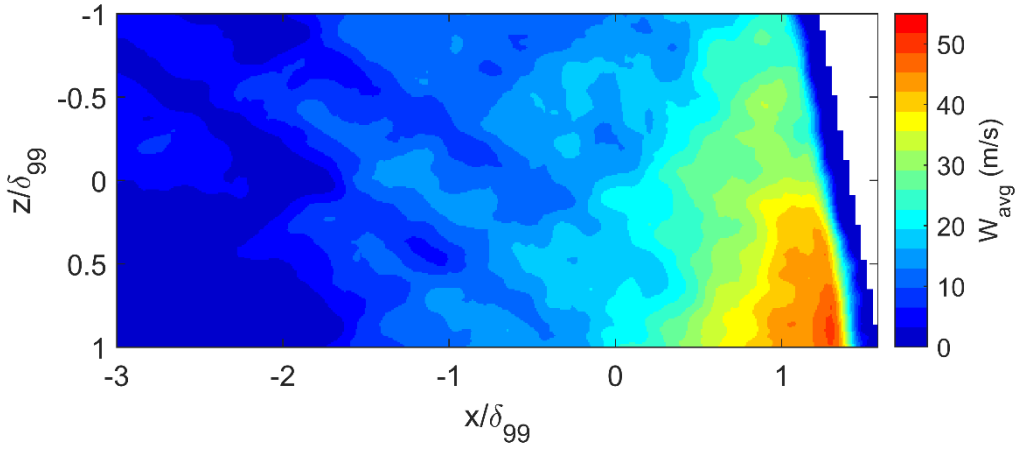
Distribution is unlimited/AFRL-2023-2280; Cleared 05/11/2023



a)



b)



c)

Figure 4.11. 10° λ_{sweep} planar PIV, ensemble-averaged crossflow velocity field with a streamwise wall-normal laser sheet. (a) y = 2 mm, (b) y = 4.5 mm, and (c) y = 8 mm.

Distribution is unlimited/AFRL-2023-2280; Cleared 05/11/2023

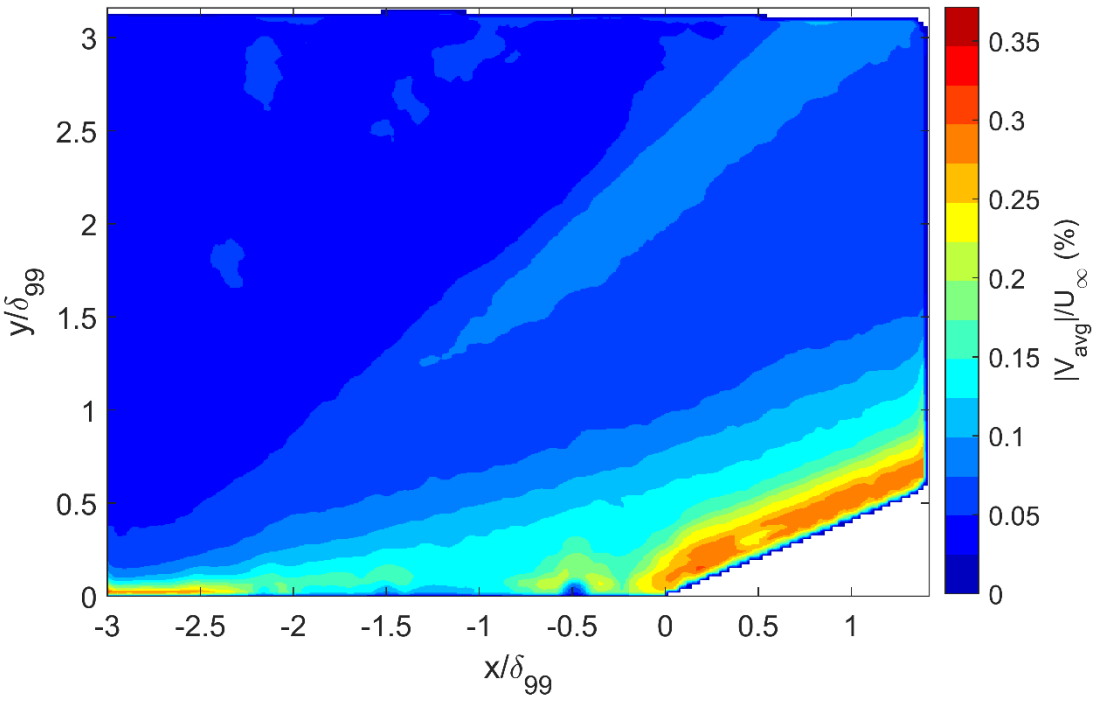
values reached up to 140 m/s, and Figure 4.10 (c) showed values up to 100 m/s. For the lower swept case, Figures 4.11 (a) and (c) had little variance with both having values up to 50 m/s. An important note made from these results was that the maximum average crossflow velocity value approximately tripled in the y = 2 mm case and approximately doubled in the y = 8 mm case when increasing the sweep from 10° to 30°. From these results, it is clear that some further work is warranted to characterize how the crossflow scales with increasing sweep angles.

4.2.3 Comparison and Statistics

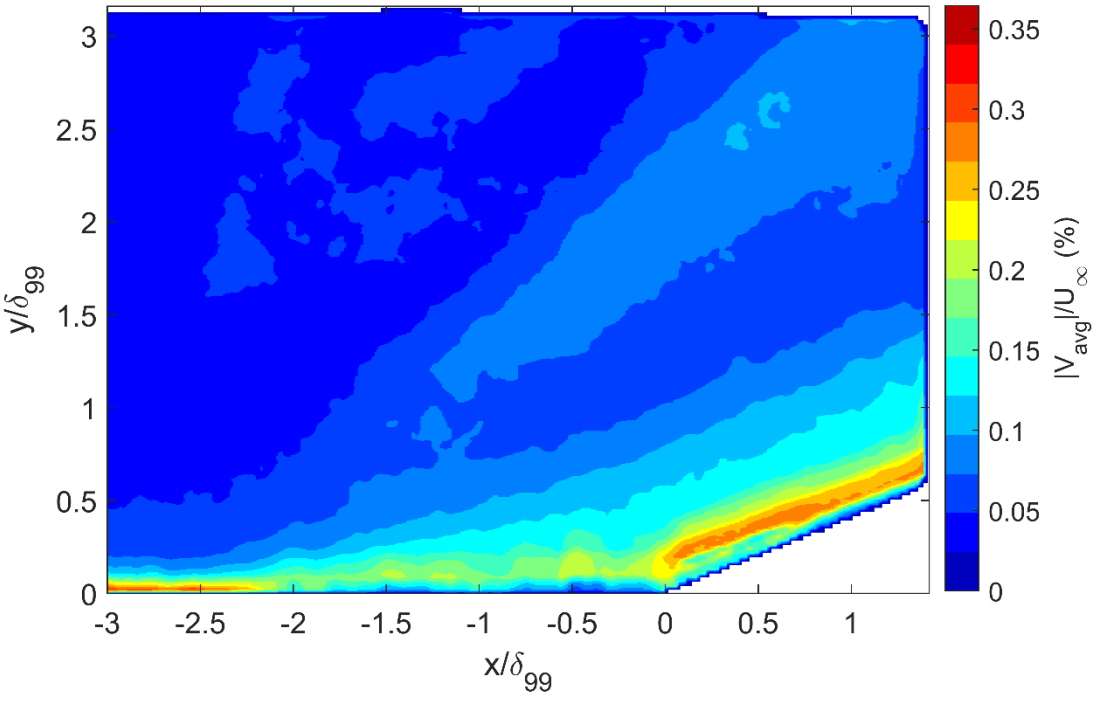
The uncertainty fields, normalized into a percentage by the velocity of the freestream flow, for the stereoscopic PIV results can be seen in Figure 4.12 for both sweep angles, and the planar PIV fields can be seen in Figure 4.13 for the 30° sweep and Figure 4.14 for the 10° sweep. These uncertainty values may seem low, but Wieneke [42] reported lower pixel error values with respect to individual functions of a number of variables (such as Gaussian pixel noise, out-of-plane motion, seeding density, and particle image size) as the interrogation windows increased in size from 16 x 16 up to 64 x 64. This investigation used a final window of 48 x 48 which could be why the uncertainty values calculated in the *a-posteriori* method were notably low up to a value of about ± 0.09% of U_∞ in the planar cases and about ± 0.37% of U_∞ in the stereoscopic cases. Albeit, the highest stereoscopic uncertainty locations were due to laser glare on the surface of the ramp. The planar and stereoscopic PIV velocity magnitude results were combined into a stacked plot as seen in Figure 4.15. The results of both PIV configurations matched one another well as can be seen by the alignment and agreement of the color contours in the stacked plots.

Upon comparing the ensemble-average crossflow velocities, W_{avg}, between stereoscopic and planar PIV, there was a slight difference in the values calculated inside the separation region. Relative to the 30° sweep stereoscopic results, the

Distribution is unlimited/AFRL-2023-2280; Cleared 05/11/2023



a)



b)

Figure 4.12. Ensemble-averaged uncertainty field of the stereoscopic PIV results for a) 30° λ_{sweep} and b) 10° λ_{sweep}.

Distribution is unlimited/AFRL-2023-2280; Cleared 05/11/2023

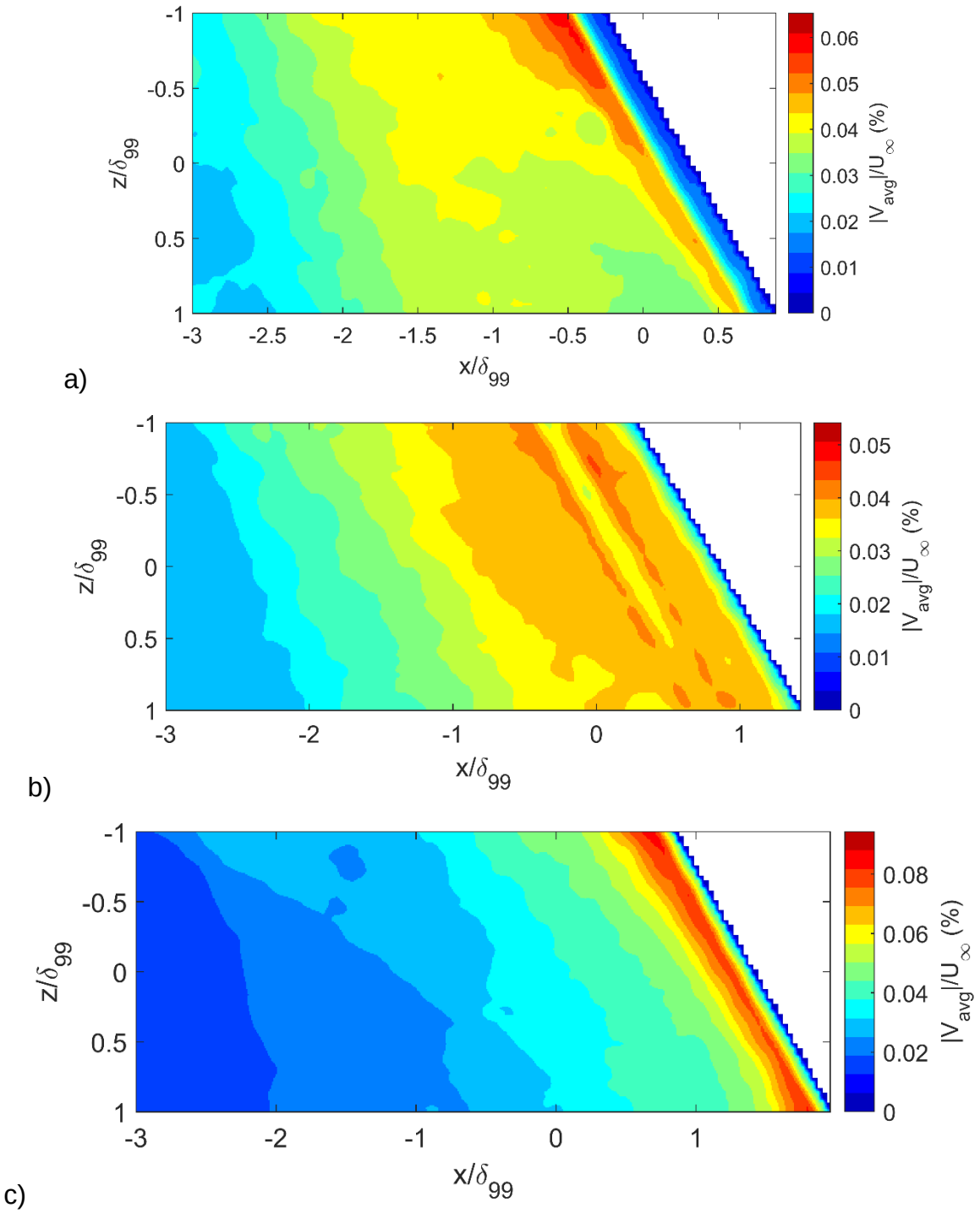


Figure 4.13. Ensemble-averaged uncertainty field of the 30° λ_{sweep} planar PIV results for a) y = 2 mm, b) y = 4.5 mm, and c) y = 8 mm.

Distribution is unlimited/AFRL-2023-2280; Cleared 05/11/2023

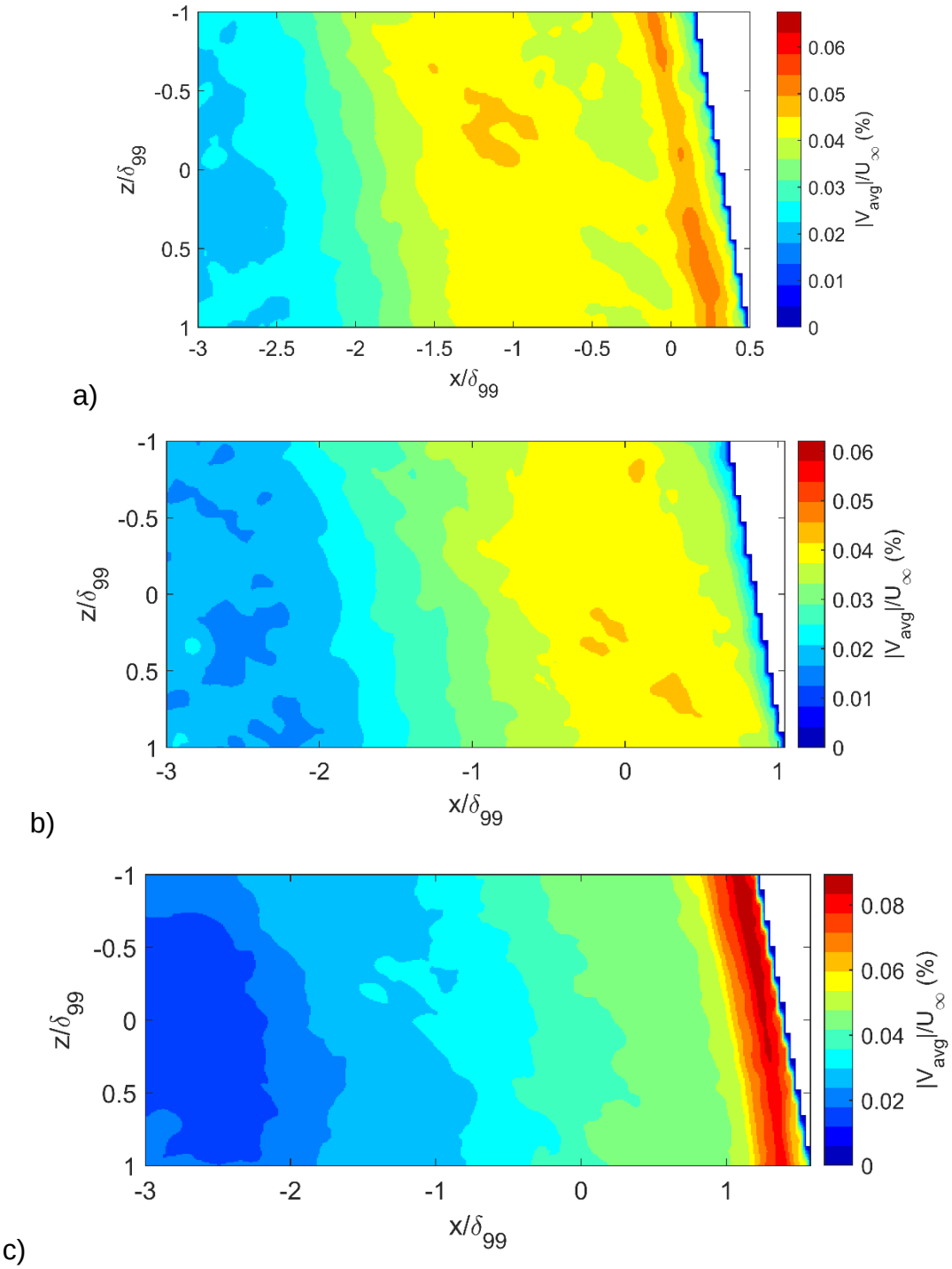
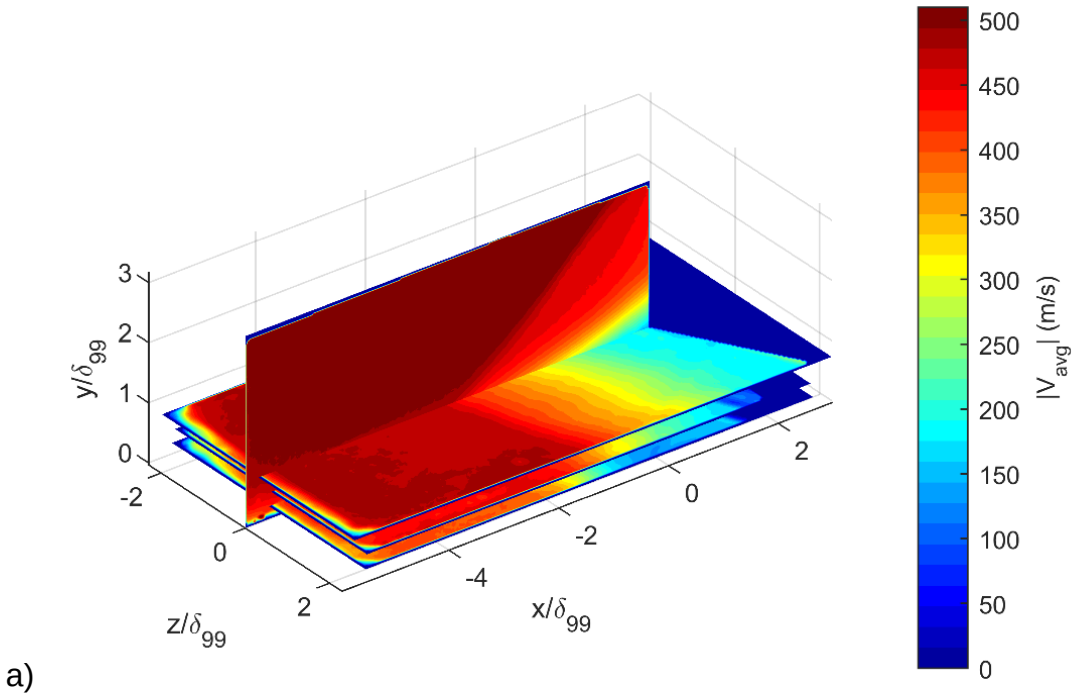
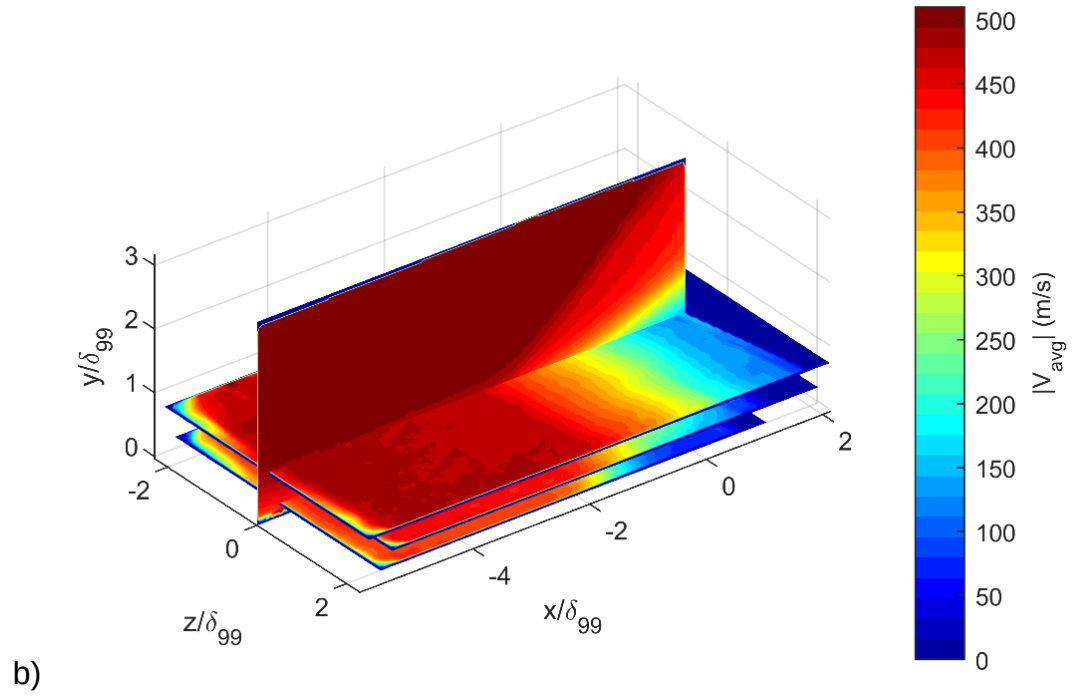


Figure 4.14. Ensemble-averaged uncertainty field of the 10° λ_{sweep} planar PIV results for a) y = 2 mm, b) y = 4.5 mm, and c) y = 8 mm.

Distribution is unlimited/AFRL-2023-2280; Cleared 05/11/2023



a)



b)

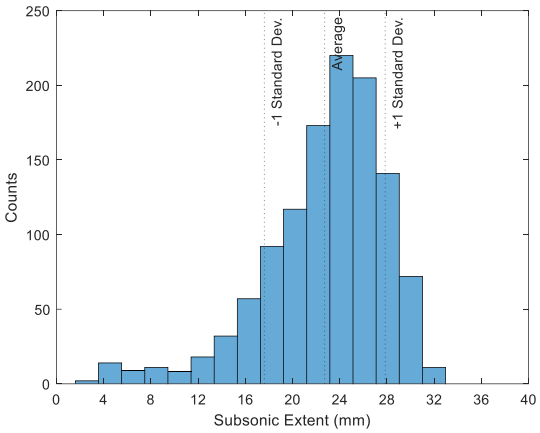
Figure 4.15. Combined planar and stereoscopic PIV figures for (a) 30° λ_{sweep} and (b) 10° λ_{sweep}.

Distribution is unlimited/AFRL-2023-2280; Cleared 05/11/2023

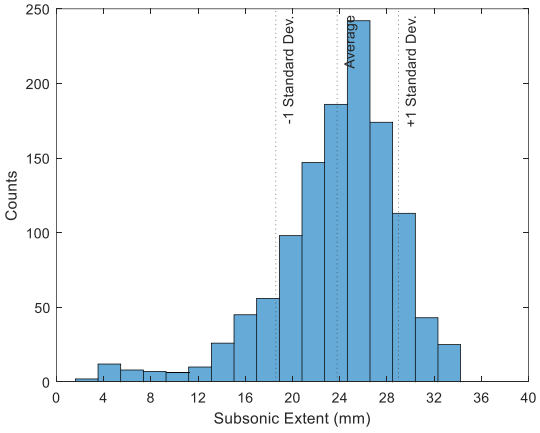
planar cases measure values that are approximately 10 m/s higher. The planar cases for the 10° sweep measure approximately 10 - 20 m/s less than the stereoscopic case. This is expected as there is more uncertainty in measuring the out-of-plane velocities for stereoscopic PIV.

Histograms in Figures 4.16 and 4.17 show the extent of subsonic flow, which is defined as the distance from the first streamwise subsonic point to the point that the laser contacts the ramp. These distances were measured along a streamwise line for each spanwise point and plotted as seen in Figures 4.8 (a) and 4.9 (a) with the blue and black dotted points. Scatter plots comparing the extent of subsonic flow and the separation distance are shown in Figures 4.18 and 4.19 to see the degree of correlation that exists between these parameters. Three locations for this analysis were selected: z/δ_{99} = -0.5, 0, and 0.5. Each data point on these plots represents the results extracted from one processed image-pair. Table 1 contains various statistical quantities (the mean, standard deviation, skewness, and kurtosis) of the histogram data. Negative skewness of these distributions illustrates that the point of separation tends towards the compression corner relative to the mean separation location for both cases; however, the skewness for the 30° case is nearly twice that of the 10° case. This implies that there are *more instances* wherein the separation scale is *smaller than* the average (i.e., the separation location is closer to the ramp) for the 30° case compared to the 10° case. The linear correlation coefficients were computed between the separation location and the subsonic extent and are shown in Table 1. A weak correlation value of ~ 0.33 was found between the subsonic extent and the size of the separation region for 30°, while the coefficients for 10° are slightly larger at ~ 0.47. This shows that there is less scatter between the beginning of flow separation and the extent of subsonic flow in the 2D separation region that exists for lower sweep than in the 3D separation region that exists for higher sweep. Although these linear correlation coefficients are lower than those expected for significant linear trends, the difference between these two values may provide some proof for

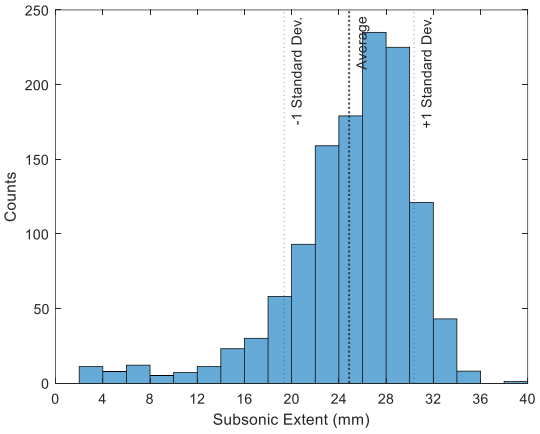
Distribution is unlimited/AFRL-2023-2280; Cleared 05/11/2023



a)



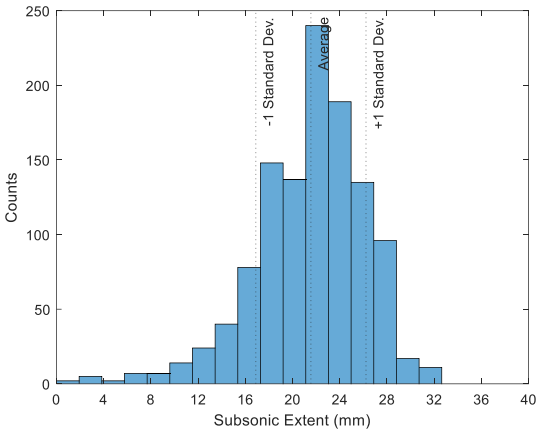
b)



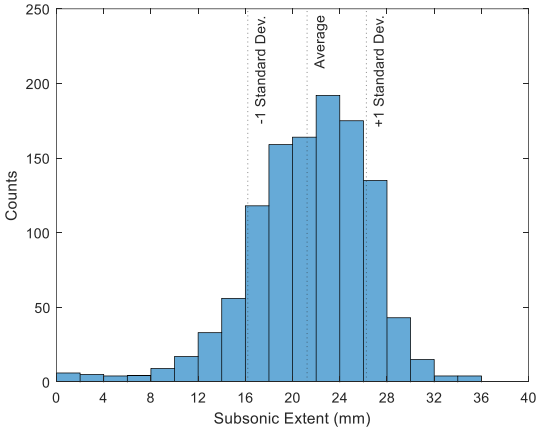
c)

Figure 4.16. Histograms of the subsonic extent along a streamwise plane leading up to the compression corner located along (a) z/δ_{99} = -0.5, (b) z/δ_{99} = 0, and (c) z/δ_{99} = 0.5 for 30° λ_{sweep} in the y = 2 mm planar PIV results.

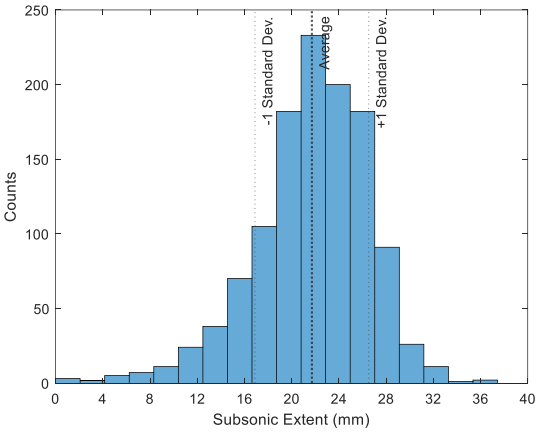
Distribution is unlimited/AFRL-2023-2280; Cleared 05/11/2023



a)



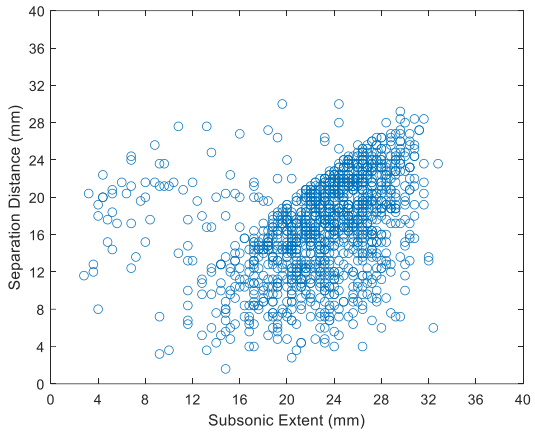
b)



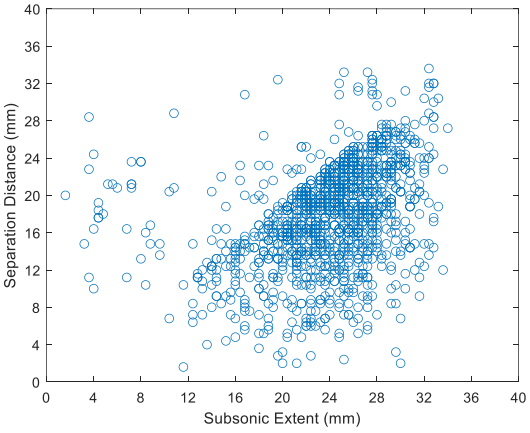
c)

Figure 4.17. Histograms of the subsonic extent along a streamwise planes leading up to the compression corner located along (a) z/δ_{99} = -0.5, (b) z/δ_{99} = 0, and (c) z/δ_{99} = 0.5 for 10° λ_{sweep} in the y = 2 mm planar PIV results.

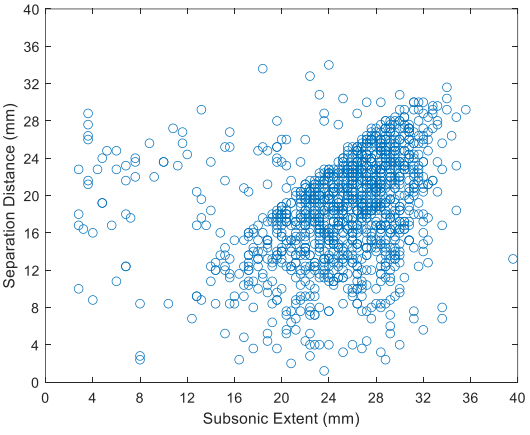
Distribution is unlimited/AFRL-2023-2280; Cleared 05/11/2023



a)



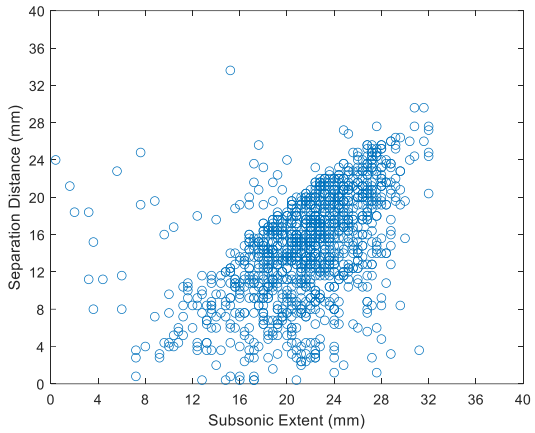
b)



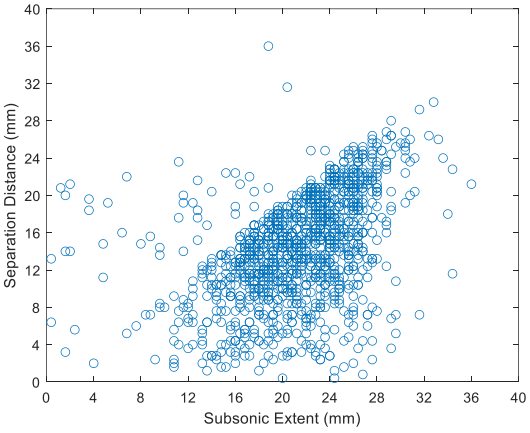
c)

Figure 4.18. Scatter plots comparing the separation location and the subsonic extent in the planar PIV y = 2 mm case at (a) z/δ_{99} = -0.5, (b) z/δ_{99} = 0, and (c) z/δ_{99} = 0.5 for 30° λ_{sweep}.

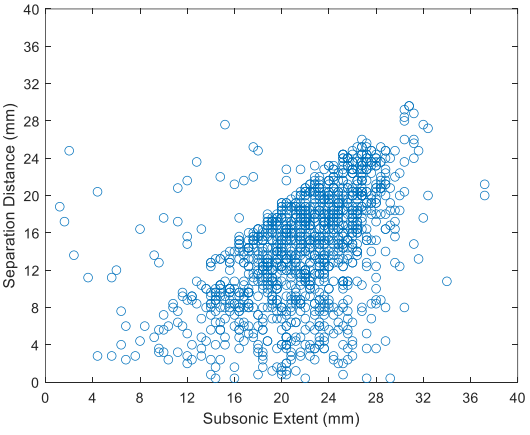
Distribution is unlimited/AFRL-2023-2280; Cleared 05/11/2023



a)



b)



c)

Figure 4.19. Scatter plots comparing the separation location and the subsonic extent in the planar PIV y = 2 mm case at (a) z/δ_{99} = -0.5, (b) z/δ_{99} = 0, and (c) z/δ_{99} = 0.5 for 10° λ_{sweep}.

Distribution is unlimited/AFRL-2023-2280; Cleared 05/11/2023

Table 1. Higher-order statistics for subsonic extent of planar PIV Data at y = 2 mm

	Mean (mm/δ_{99})	Standard Deviation (±mm/δ_{99})	Skewness	Kurtosis	Linear Correlation Coefficient between Separation Distance & Subsonic Extent
z/δ_{99} = 0.5 30° sweep	2.22	0.49	-1.45	6.06	0.28
z/δ_{99} = 0.5 10° sweep	1.94	0.43	-0.72	4.33	0.48
z/δ_{99} = 0 30° sweep	2.13	0.46	-1.15	5.26	0.37
z/δ_{99} = 0 10° sweep	1.89	0.45	-0.78	4.65	0.44
z/δ_{99} = -0.5 30° sweep	2.03	0.46	-1.15	4.94	0.35
z/δ_{99} = -0.5 10° sweep	1.92	0.42	-0.85	4.64	0.49

Distribution is unlimited/AFRL-2023-2280; Cleared 05/11/2023

the hypothesis regarding the extent of subsonic flow and its relationship with the size of the separation regions.

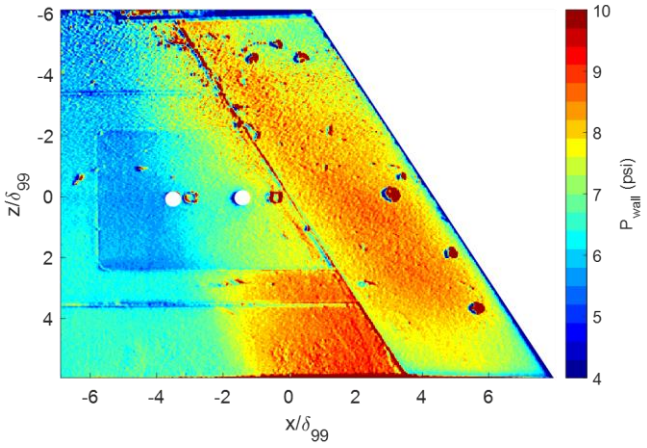
4.3 Unsteady Pressure Sensitive Paint

Results from the PSP measurements are shown in Figures 4.20 (a, b) and 4.21 (a, b) which contain contour plots of the wall pressures ensemble-averaged over 2000 frames. The root mean square of the fluctuating pressures, P'_{rms}, were also computed at each point and have been plotted in Figures 4.20 (c) and 4.21 (c). Intensity variations within the images and between cases result from differences in the application of the PSP top coat and differences in the underlying material. It appears that the central filament-printed floor insert caused a brighter response, which converts to a lower calculated pressure of ~ 1 psi, as compared with the metal tunnel floor and resin printed ramps. Since PSP calibration is temperature dependent, different thermal characteristics of the substrate materials may cause this variation. Regardless of this effect, the spectra computed from the PSP data are in very good agreement with the pressure spectra computed from the Kulite pressure transducers.

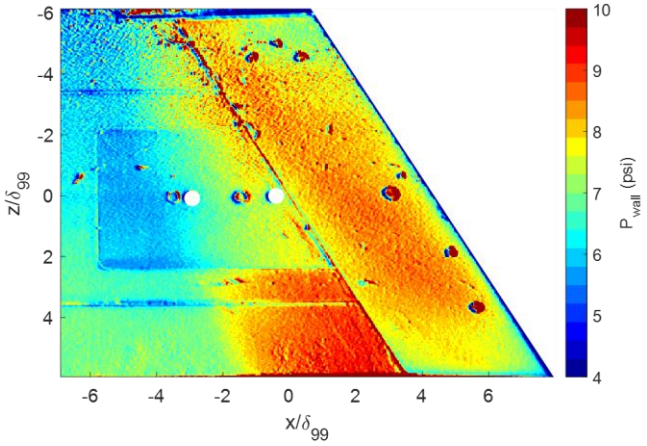
A trace along a horizontal line (i.e., parallel to the incoming flow) directly below the pressure taps in the P'_{rms} images are displayed in Figure 4.22. Comparing the P'_{rms} between the two graphs in Figure 4.22 agrees with the results of Erengil and Dolling [20] in that the standard deviation of the pressure values is greater in the lesser swept case. Further, the general shape of these curves agrees well with P' traces from previous data of a turbulent 2D SBLI over an unswept ramp [9].

The power spectral densities (PSDs) of P' were computed from a set of 2000 images at specific regions of interest located closely below each pressure tap, and PSDs of the pressure transducers (using data from throughout the entire

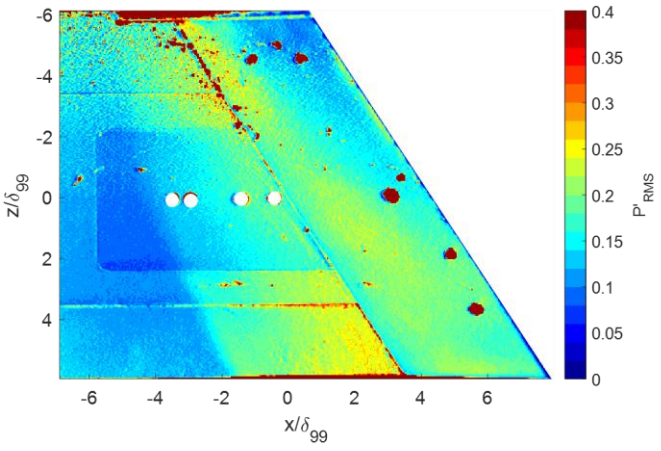
Distribution is unlimited/AFRL-2023-2280; Cleared 05/11/2023



a)



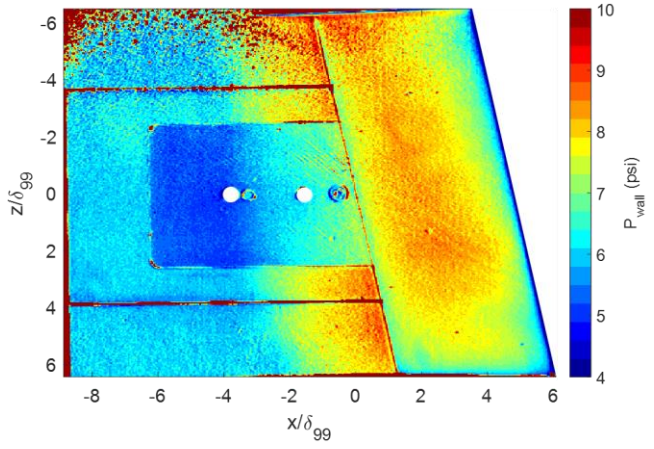
b)



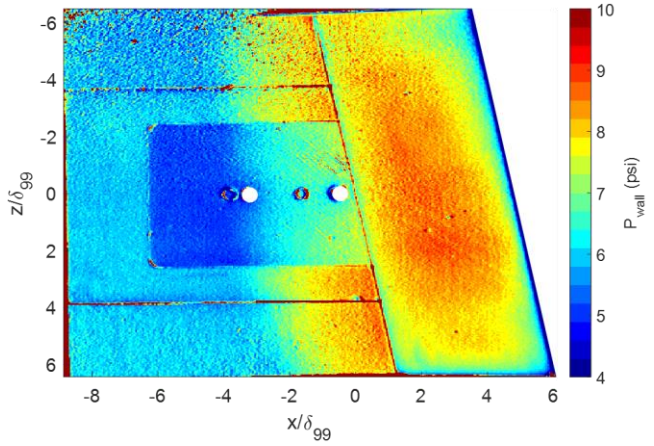
c)

Figure 4.20. PSP pressure fields for (a) case 1 and (b) case 2 along with the (c) P'_{rms} values in psi at 30° λ_{sweep}.

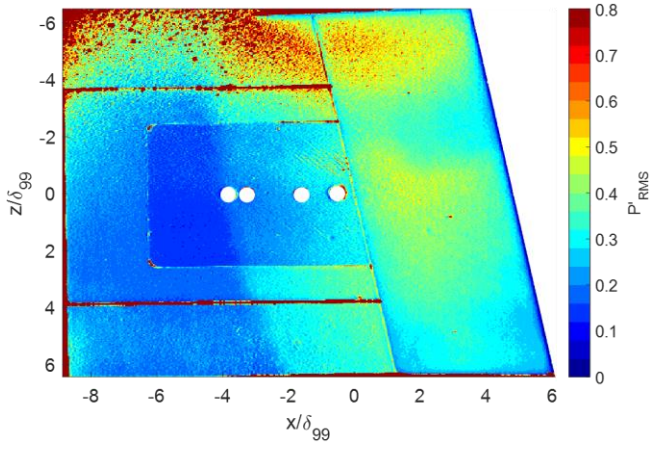
Distribution is unlimited/AFRL-2023-2280; Cleared 05/11/2023



a)



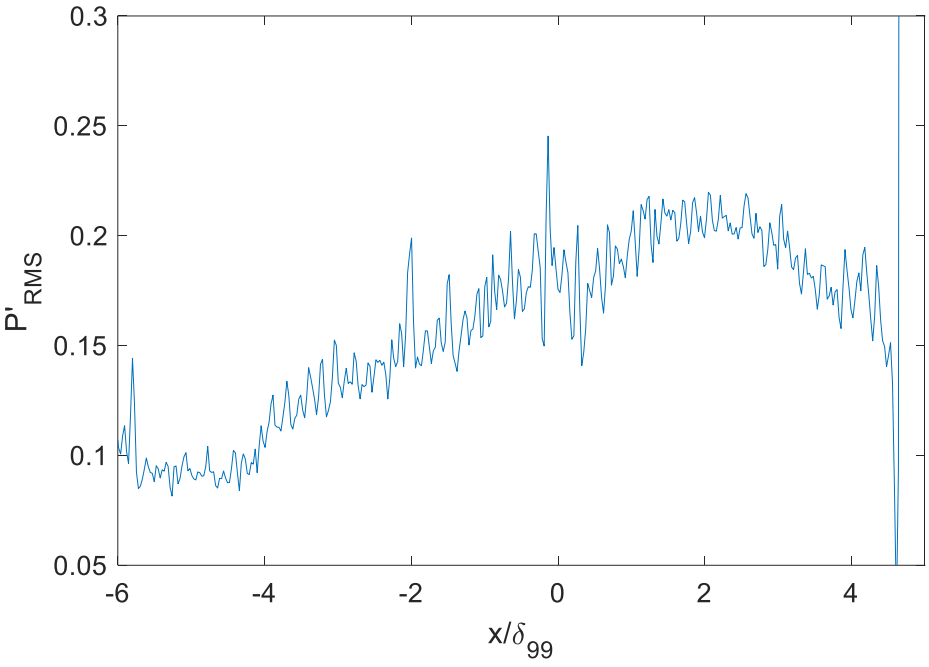
b)



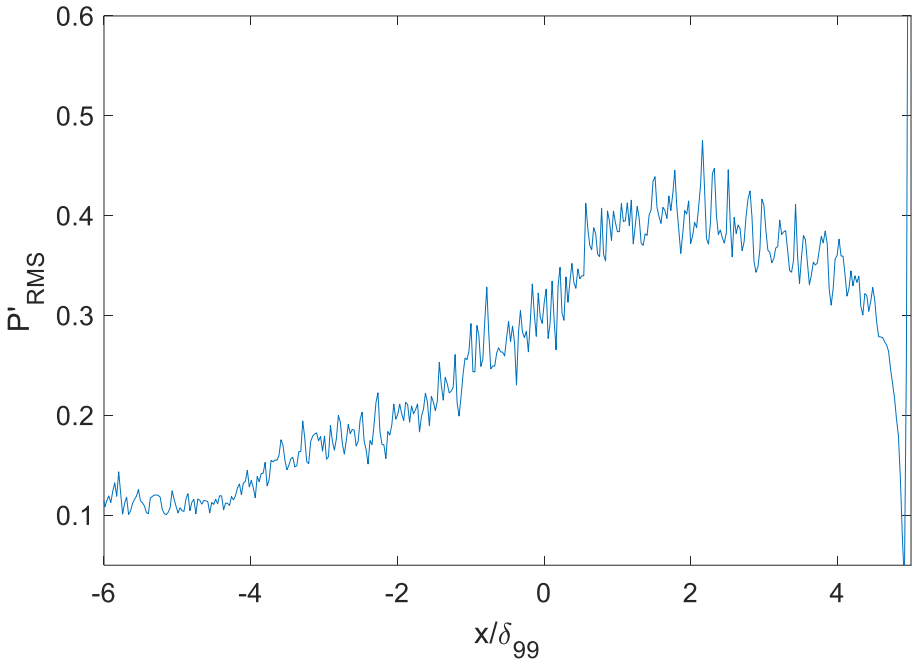
c)

Figure 4.21. PSP pressure fields for (a) case 1 and (b) case 2 along with the (c) P'_{rms} in psi values at 10° λ_{sweep}.

Distribution is unlimited/AFRL-2023-2280; Cleared 05/11/2023



a)



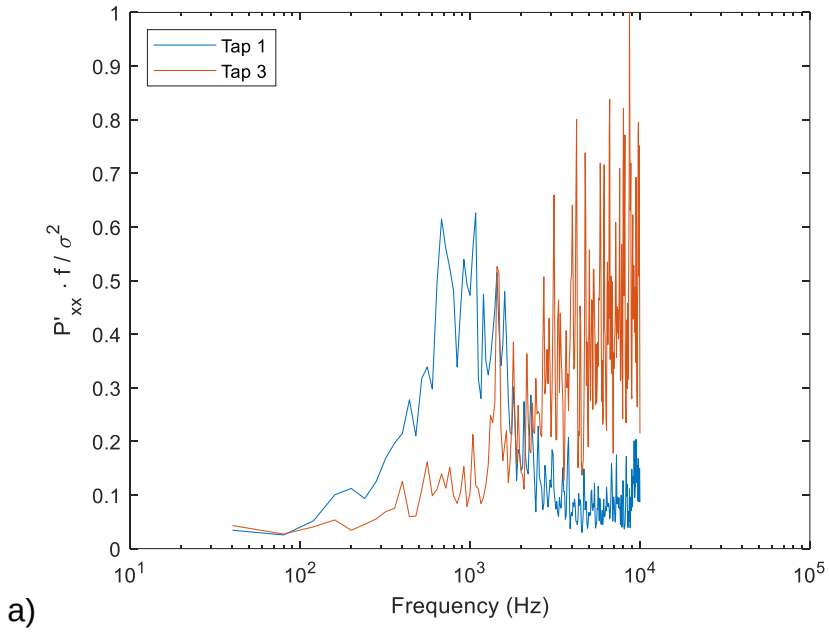
b)

Figure 4.22. Trace of the PSP-computed P'_{rms} values for (a) 30° λ_{sweep} and (b) 10° λ_{sweep} calculated along a horizontal line located at z/δ_{99} = 0.49 (directly below the line of pressure taps).

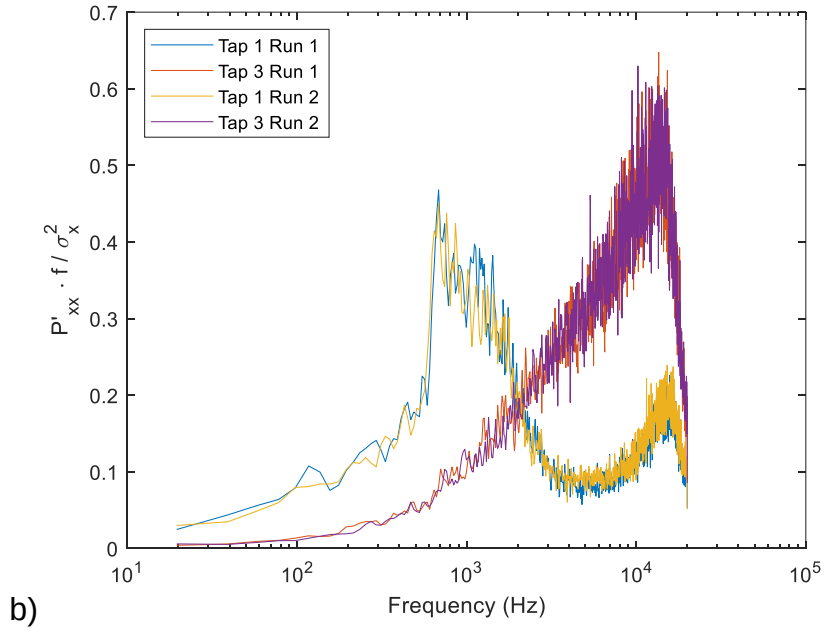
Distribution is unlimited/AFRL-2023-2280; Cleared 05/11/2023

run of 80000 samples) are displayed in Figures 4.23, 4.24, 4.25, and 4.26. The pressure taps were located at $3.5\delta_{99}$ denoted as Tap 1 and Set $3.5\delta_{99}$, $3\delta_{99}$ denoted as Tap 2 and Set $3\delta_{99}$, $1.5\delta_{99}$ denoted as Tap 3 and Set $1.5\delta_{99}$, and $0.5\delta_{99}$ denoted as Tap 4 and Set $0.5\delta_{99}$, whereas the run number denotes which of the four tunnel runs the data was processed from. The data in Figures 4.23 and 4.24 correspond to the spectra obtained from the 30° sweep case, while those shown in Figures 4.25 and 4.26 are for that of 10° sweep. For these figures, the top plot (a) was computed from the PSP data while the bottom plot (b) was computed from the pressure transducers. The PSDs for the PSP images and the pressure transducer data agree well with their respective cases. It should be noted that the pressure spectra have been pre-multiplied by the frequency vector and non-dimensionalized by the variance. Dominant frequencies in the separation region are due to the movement of the separation shock [20]. For the highly swept case, the peak appears to be between 0.7 to 2.2 kHz near the upstream side of the separation region (tap locations 1 and 2), while 8 to 15 kHz dominates downstream, near the ramp face (tap locations 3 and 4). For the lower swept case, the dominant frequency in the start of the separation region appears to be about 0.7 kHz, while the high frequencies from about 8 to 15 kHz dominate the spectra near the ramp. From the results in the beginning of the separation region, it is clear that the unsteadiness frequency increases as the sweep increases. For Mach 5 flow at 30° sweep with a compression angle of 28° (from Erengil and Dolling [20]), dominant frequencies range from about 3 to 6 kHz along a line extending through most of the separation region but oriented to be normal to the sweep angle. Under these same conditions but with a 10° sweep, dominant frequencies are about 0.9 to 1.5 kHz [20]. The differences between the present results and those in Erengil and Dolling [20] are likely due to the different Mach number or the different compression angles. However, the general range and similar offset between the high and low sweep cases with respect to their counterparts in prior studies do seem to compare well.

Distribution is unlimited/AFRL-2023-2280; Cleared 05/11/2023



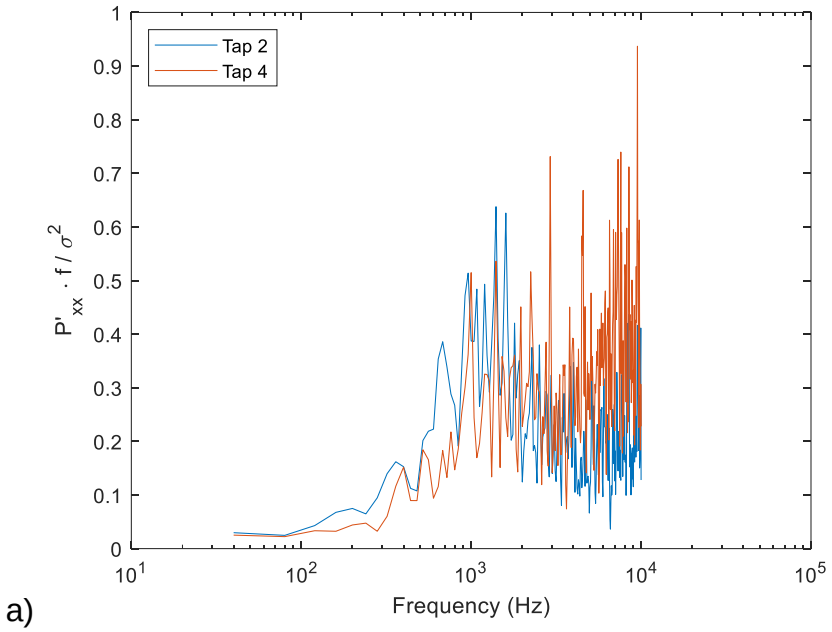
a)



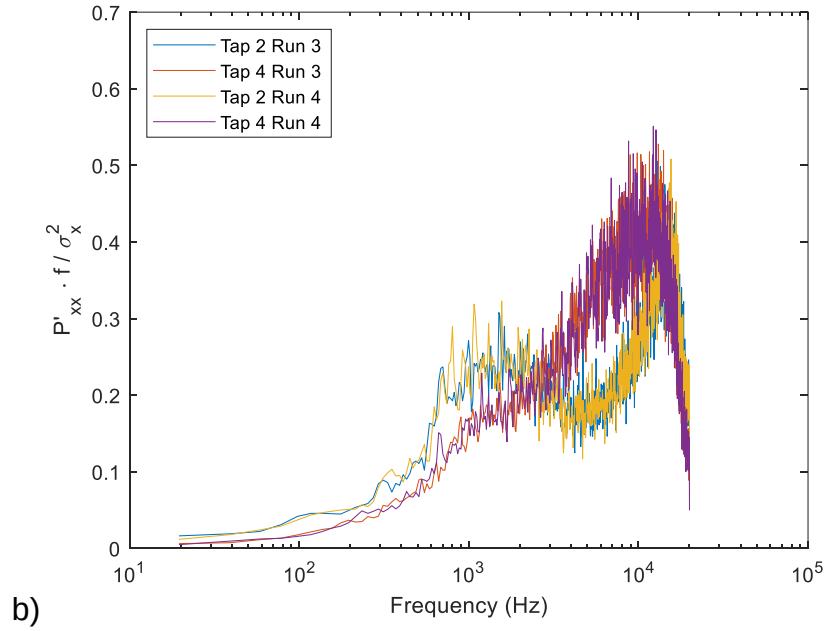
b)

Figure 4.23. Case 1 for the 30° λ_{sweep}: (a) PSDs of *P'* values from PSP images investigated directly below each pressure tap for tap positions 1 and 3, and (b) PSDs of the Kulite transducers.

Distribution is unlimited/AFRL-2023-2280; Cleared 05/11/2023



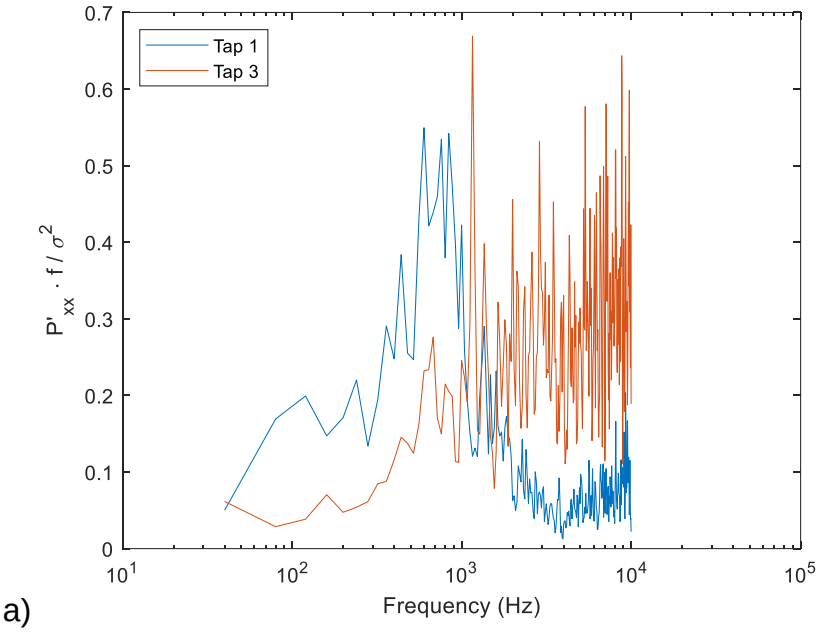
a)



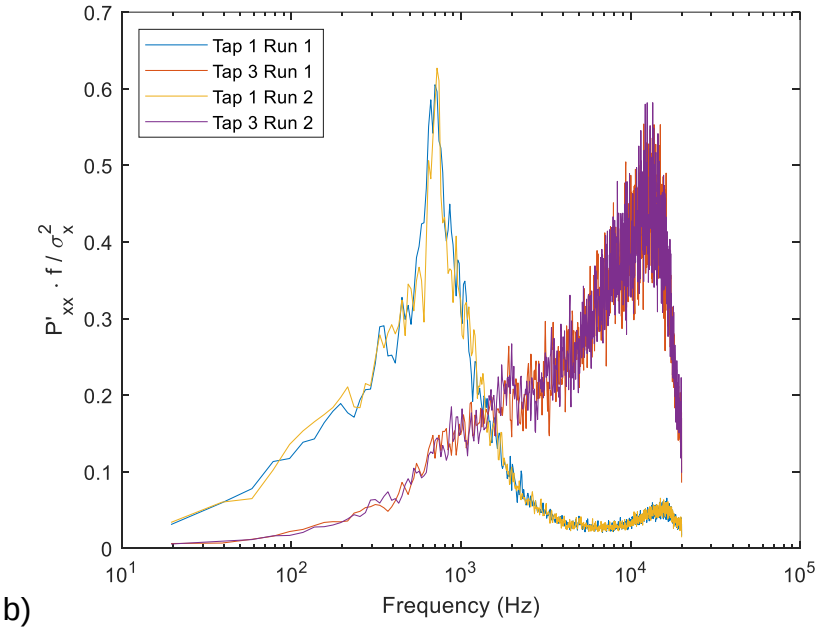
b)

Figure 4.24. Case 2 for the 30° λ_{sweep}: (a) PSDs of *P'* values from PSP images investigated directly below each pressure tap for tap positions 2 and 4, and (b) PSDs of the Kulite transducers.

Distribution is unlimited/AFRL-2023-2280; Cleared 05/11/2023



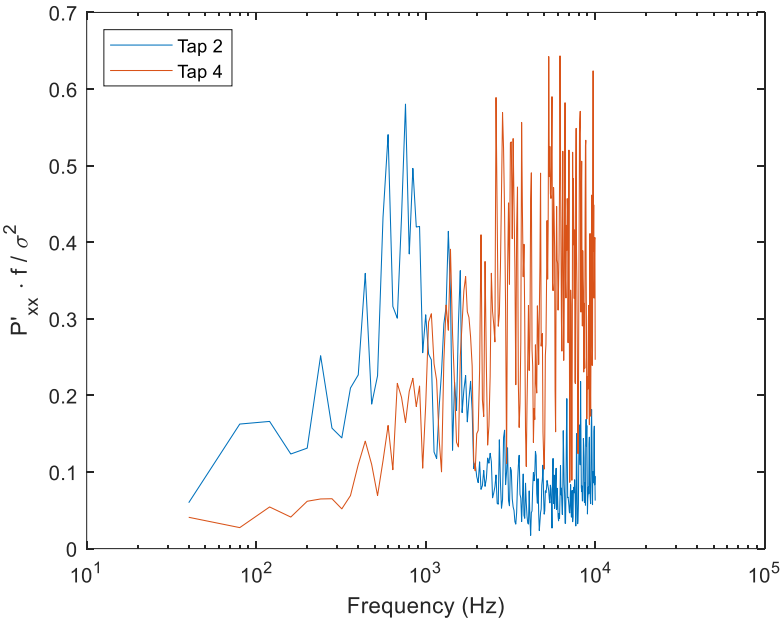
a)



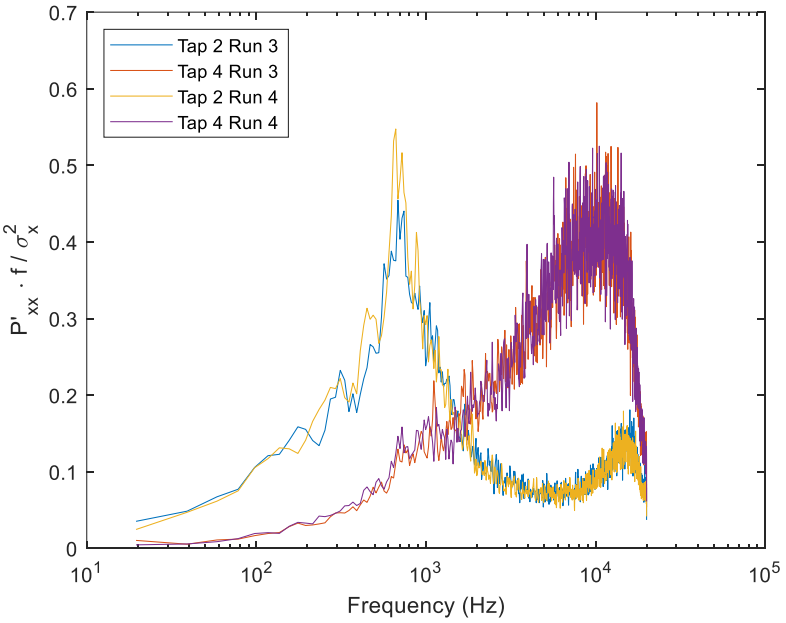
b)

Figure 4.25. Case 1 for 10° λ_{sweep}: (a) PSDs of P' values from PSP images investigated directly below each pressure tap for tap positions 1 and 3, and (b) PSDs of the Kulite transducers.

Distribution is unlimited/AFRL-2023-2280; Cleared 05/11/2023



a)



b)

Figure 4.26. Case 2 for 10° λ_{sweep}: (a) PSDs of P' values from PSP images investigated directly below each pressure tap for tap positions 2 and 4, and (b) PSDs of the Kulite transducers.

Distribution is unlimited/AFRL-2023-2280; Cleared 05/11/2023

CHAPTER 5
CONCLUSIONS

The aim of this study was to understand the role that the extent of subsonic flow within the separation bubble plays in the unsteadiness of swept shock/turbulent boundary layer interactions and also to compare the 3D and approximately 2D interactions generated by highly swept and low swept compression ramps, respectively. Fluorescent oil flow visualization, stereoscopic and planar particle image velocimetry, and unsteady pressure sensitive paint were conducted on two compression ramps with differing sweep angles of 30° and 10° at Mach 2 freestream conditions. In every diagnostic except for stereoscopic particle image velocimetry, the quasi-conical symmetry of the separation region for the 30° sweep and the quasi-cylindrical symmetry for the 10° sweep were observed.

The different flow fields were compared with oil flow and particle image velocimetry. Oil flow over the 30° sweep showed an average separation location to be $x_{sep} \sim -1.9\delta_{99}$ along the centerline relative to the compression corner and $x_{sep} \sim 1.4\delta_{99}$ over the 10° sweep, resulting in a difference of $\Delta x_{sep} \sim 0.5\delta_{99}$ between the two ramps. In stereoscopic PIV, the intersection of the shock with the tunnel floor in the averaged images yielded $x_{sep} \sim -2.7\delta_{99}$ for the 30° sweep and $x_{sep} \sim -2.5\delta_{99}$ for the 10° sweep showing a difference of about $0.2\delta_{99}$ in the average separation locations between the two cases. From the planar PIV data, the streamwise separation location, subsonic extent, and crossflow velocities were analyzed. From the heights of y = 2 mm to y = 8 mm inside the boundary layer and normal to the floor, the average crossflow velocities, W_{avg}, approximately doubled in the 10° swept case and approximately tripled in the 30° swept case. Scatter plots of the separation location and the extent of subsonic flow showed that the linear correlation coefficient was positive between these two parameters. In considering the correlation at three separate spanwise locations, the 30° sweep resulted in an average linear correlation coefficient of ~0.33 while the 10° sweep resulted in a

Distribution is unlimited/AFRL-2023-2280; Cleared 05/11/2023

coefficient of ~0.47. While both of these coefficients are low, the difference between the two is noteworthy. The highly swept case had a lower value, indicating that the likelihood of a linear trend existing between these two parameters is higher for the case with less sweep (i.e., where cylindrical symmetry exists). This provides some evidence to the hypothesis that the subsonic extent is directly related to the size of the separation region; however, these values are not as high as expected.

The unsteadiness was compared between the two different sweep cases using PSP along with 4 pressure transducers located along the centerline. For the highly swept case, dominant frequencies due to movement of the separation shock foot appear to be between 0.7 to 2.2 kHz near the upstream side of the separation region, while 8 to 15 kHz dominates downstream closer to the ramp. For the lower swept case, the dominant frequency in the start of the separation region appears to be about 0.7 kHz, and the dominant frequencies nearing the ramp appear to be about 8 to 15 kHz. It appears that the unsteadiness increases to higher frequencies with increasing sweep.

Future experiments are planned at Mach 4 conditions in UTSI's 24" x 24" Mach 4 Ludwieg tube [46]. Further data will be recorded through the use of uPSP and acetone molecular tagging velocity with the focus of the research being in the area of the separation region where subsonic flow is present in the swept shock/boundary layer interaction.

Distribution is unlimited/AFRL-2023-2280; Cleared 05/11/2023

REFERENCES

[1] Anderson, J. D., *Hypersonic Shock-Wave/Boundary-Layer Interactions*, Hypersonic and High-Temperature Gas Dynamics, Second Edition., American Institute of Aeronautics and Astronautics, 2006.

[2] Dolling, D. S., “Fifty Years of Shock-Wave/Boundary-Layer Interaction Research: What Next?” *AIAA Journal*, Vol. 39, No. 8, pp. 1517–1531, 2001.

[3] Bertin, J. J., and Cummings, R. M., “Fifty years of hypersonics: where we’ve been, where we’re going,” *Progress in Aerospace Sciences*, Vol. 39, No. 6, pp. 511-536, 2003.

[4] Curry, M., and Dunbar, B., “X-15 Fact Sheet,” NASA Dryden Flight Research Center, 2008.

[5] Gibbs, Y., “NASA Armstrong Fact Sheet: Hyper-X Program,” NASA, 2014.

[6] “APFSDS 120mm Armor Piercing Fin Stabilized Discarding Sabot,” www.militaryimages.net, 2008.

[7] Allen, D. S., Langley, K. R., Schmisseur, J. D., and Kreth, P. A., “Separation Region Unsteadiness Drivers in Swept Compression Ramps,” AIAA SciTech Forum, 2023.

[8] Andreopoulos, Y., Agui, J. H., and Briassulis, G., “Shock Wave-Turbulence Interaction” *Annual Review of Fluid Mechanics*, Vol. 32, pp. 309-345, 2000.

[9] Erengil, M. E., and Dolling, D. S., “Unsteady Wave Structure near Separation in a Mach 5 Compression Ramp Interaction,” *AIAA Journal*, Vol. 29, No. 5, pp. 728-735, 1991.

[10] Beresh, S. J., Clemens, N. T., and Dolling, D. S., “Relationship Between Upstream Turbulent Boundary-Layer Velocity Fluctuations and Separation Shock Unsteadiness,” *AIAA Journal*, Vol. 40, No. 12, pp. 2412-2422, 2002.

Distribution is unlimited/AFRL-2023-2280; Cleared 05/11/2023

[11] Ganapathisubramani, B., Clemens, N. T., and Dolling, D. S., “Effects of upstream boundary layer on the unsteadiness of shock-induced separation,” *Journal of Fluid Mechanics*, Vol. 585, pp. 369-394, 2007.

[12] Ganapathisubramani, B., Clemens, N. T., and Dolling, D. S., “Low-frequency dynamics of shock-induced separation in a compression ramp interaction,” *Journal of Fluid Mechanics*, Vol. 636, pp. 397-425, 2009.

[13] Dupont, P., Haddad, C., Debieve, J., “Space and time organization in a shock-induced separated boundary layer,” *Journal of Fluid Mechanics*, Vol. 559, pp. 255-277, 2006.

[14] Pirozzoli, S., and Grasso, F., “Direct numerical simulation of impinging shock wave/turbulent boundary layer interaction at *M*=2.25,” *Physics of Fluids*, Vol. 18, No. 6, pp. 065113, 2006.

[15] Pipponiau, S., Dussauge, J. P., Debieve, J. F., and Dupont, J. F., “A simple model for low-frequency unsteadiness in shock-induced separation,” *Journal of Fluid Mechanics*, Vol. 629, pp. 87-108, 2009.

[16] Touber, E., and Sandham, N. D., “Low-Order Stochastic Modelling of Low-Frequency Motions in Reflected Shock-Wave/Boundary-Layer Interactions,” *Journal of Fluid Mechanics*, Vol. 671, pp. 417-465, 2011.

[17] Clemens, N. T., and Narayanaswamy, V., “Low-Frequency Unsteadiness of Shock Wave/Turbulent Boundary Layer Interactions,” *Annual Review of Fluid Mechanics*, Vol. 46, pp. 469-492, 2014.

[18] Priebe, S., and Martin, M. P., “Low-frequency unsteadiness in shock wave-turbulent boundary layer interaction,” *Journal of Fluid Mechanics*, Vol. 699, pp. 1-49, 2012.

[19] Poggie, J., Bisek, N. J., and Kimmel, R. L., “Spectral Characteristics of Separation Shock Unsteadiness,” *AIAA Journal*, Vol. 53, No. 1, pp. 200-214, 2015.

[20] Erengil, M. E., and Dolling, D. S., “Effect of Sweepback on Unsteady Separation in Mach 5 Compression Ramp Interactions,” *AIAA Journal*, Vol. 31, No. 2, pp. 302–311, 1993.

Distribution is unlimited/AFRL-2023-2280; Cleared 05/11/2023

[21] Arora, N., Ali, M. Y., Zhang, Y., and Alvi, F. S., “Shock-Boundary Layer Interaction due to a Sharp Unswept Fin in a Mach 2 Flow,” AIAA SciTech Forum, 2015.

[22] Schmisseur, J. D., and Dolling, D. S., “Fluctuating Wall Pressures near Separation in Highly Swept Turbulent Interactions,” *AIAA Journal*, Vol. 32, No. 6, pp. 1151-1157, 1994.

[23] Padmanabhan, S., Maldonado, J. C., Threadgill, J. A. S., and Little, J. C., “Experimental Study of Swept Impinging Oblique Shock/Boundary-Layer Interaction,” *AIAA Journal*, Vol. 59, No. 1, pp. 140-149, 2021.

[24] Settles, G. S., Perkins, J. J., and Bogdonoff, S. M., “Investigation of Three-Dimensional Shock/Boundary-Layer Interactions at Swept Compression Corners,” *AIAA Journal*, Vol. 18, No. 7, pp. 779-785, 1980.

[25] Settles, G. S., and Teng, H-Y., “Cylindrical and Conical Flow Regimes of Three-Dimensional Shock/Boundary-Layer Interactions,” *AIAA Journal*, Vol. 22, No. 2, pp. 194-200, 1982.

[26] Alvi, F. S., and Settles, G. S., “Physical Model of the Swept Shock Wave/Boundary-Layer Interaction Flowfield,” *AIAA Journal*, Vol. 30, No. 9, pp. 2252-2258, 1992.

[27] Vanstone, L., Saleem, M., Seckin, S., and Clemens, N. T., “Experimental Investigation of Unsteadiness of Swept-Ramp Shock/Boundary Layer Interactions at Mach 2,” AIAA Aerospace Sciences Meeting, 2015.

[28] Vanstone, L., Saleem, M., Seckin, S., and Clemens, N. T., “Effect of Upstream Boundary Layer of Unsteadiness of Swept-Ramp Shock/Boundary Layer Interactions at Mach 2,” AIAA Aerospace Sciences Meeting, 2016.

[29] Vanstone, L., Musta, M. N., Seckin, S., and Clemens, N. T., “Experimental study of the mean structure and quasi-conical scaling of a swept-compression-ramp interaction at Mach 2,” *Journal of Fluid Mechanics*, Vol. 841, pp. 1–27, 2018.

Distribution is unlimited/AFRL-2023-2280; Cleared 05/11/2023

[30] Vanstone, L., and Clemens, N. T., “POD Analysis of Unsteadiness Mechanisms within a Swept Compression-Ramp Shock-Wave Boundary-Layer Interaction at Mach 2,” AIAA SciTech Forum, 2018.

[31] Vanstone, L., and Clemens, N. T., “Unsteadiness Mechanisms of a Swept Compression-Ramp Shock/Boundary Layer Interaction at Mach 2,” AIAA SciTech Forum, 2019.

[32] Vanstone, L., Goller, T., Clemens, N. T., and Mears, L. J., “Separated Flow Unsteadiness in a Mach 2 Swept Compression-Ramp Interaction using High-Speed PSP,” AIAA Aviation Forum, 2019.

[33] Gonzalez, D. R., Adler, M. C., and Gaitonde, D. V., “Dynamical Structures in a Swept Compression Ramp Shock/Turbulent-Boundary-Layer Interaction,” 23rd AIAA Computational Fluid Dynamics Conference, 2017.

[34] Adler, M. C., and Gaitonde, D. V., “Dynamics of strong swept-shock/turbulent-boundary-layer interactions,” *Journal of Fluid Mechanics*, Vol. 896, pp. A29, 2020.

[35] Adler, M. C., and Gaitonde, D. V., “Flow Similarity in Strong Swept-Shock/Turbulent-Boundary-Layer Interactions,” *AIAA Journal*, Vol. 57, No. 4, pp. 1579-1593, 2019.

[36] Adler, M. C., and Gaitonde, D. V., “Unsteadiness in Swept-Compression-Ramp Shock/Turbulent-Boundary-Layer Interactions,” 55th AIAA Aerospace Sciences Meeting, pp. 1–12, 2017.

[37] Holst, K. R., and Schmisseur, J. D., “Reynolds-Averaged Navier-Stokes Simulations of Shock Boundary Layer Interactions from Swept Compression Ramps at Mach 2 and 5,” 46th AIAA Fluid Dynamics Conference, 2016.

[38] Adler, M. C., and Gaitonde, D. V., “Influence of separation structure on the dynamics of shock/turbulent-boundary-layer interactions,” *Theoretical and Computational Fluid Dynamics*, Vol. 36, No. 2, pp. 303-326, 2022.

[39] Goonko, Y. P., Latypov, A. F., Mazhul, I. I., Kharitonov, A. M., Yaroslavtsev, M. I., and Rostand, P., “Structure of Flow over a Hypersonic

Distribution is unlimited/AFRL-2023-2280; Cleared 05/11/2023

Inlet with Side Compression Wedges," *AIAA Journal*, Vol. 41, No. 3, pp. 436-447, 2003.

[40] Kocher, B. D., "Characterizing the Streamwise Development of Surface Roughness Effects on a Supersonic Boundary Layer," Master's thesis, Department of Mechanical, Aerospace, and Biomedical Engineering, University of Tennessee, Knoxville, TN, 2018.

[41] Adrian, R. J., and Westerweel, J., Particle Image Velocimetry, Cambridge University Press, 2011.

[42] Wieneke, B., "PIV uncertainty quantification from correlation statistics," *Measurement Science and Technology*, Vol. 26, No. 7, Paper 074002, 2015.

[43] Neal, D. R., Sciacchitano, A., Smith, B. L., and Scarano, F., "Collaborative framework for PIV uncertainty quantification: the experimental database," *Measurement Science and Technology*, Vol. 26, No. 7, Paper 074003, 2015.

[44] Sciacchitano, A., Neal, D. R., Smith, B. L., Warner, S. O., Vlachos, P. P., Wieneke, B., and Scarano, F., "Collaborative framework for PIV uncertainty quantification: comparative assessment of methods," *Measurement Science and Technology*, Vol. 26, No. 7, Paper 074004, 2015.

[45] Sciacchitano, A., and Wieneke, B., "PIV uncertainty propagation," *Measurement Science and Technology*, Vol. 27, No. 8, Paper 084006, 2016.

[46] Kreth, P. A., Gragston, M., Davenport, K., and Schmisseur, J. D., "Design and Initial Characterization of the UTSI Mach 4 Ludwieg Tube," AIAA SciTech Forum, 2021.

Distribution is unlimited/AFRL-2023-2280; Cleared 05/11/2023

VITA

Daniel S. Allen was born and raised near Knoxville, TN and was essentially raised in the Great Smoky Mountains National Park. He studied Aerospace Engineering at the University of Tennessee, Knoxville (UTK) and earned his Bachelor's of Science degree in the spring of 2020. In his time as an undergraduate student, he spent most of his free time working at a restaurant to survive or practicing and competing across the country with the Gymnastics Club at UTK while serving as the Treasurer of the club. In the summer of 2019 he participated in an internship at the University of Tennessee Space Institute (UTSI). He enrolled as a Graduate Research Assistant at UTSI in fall of 2020 working and earned his Master's of Science degree in spring of 2023 after two and a half years of living through a pandemic. During his time in graduate school, he fell in love with the sport of rock climbing and plans to chase his dream of crushing hard climbing routes up the tallest of cliffs and subsequently skydiving off of them. After graduating, he is entering into the job field focused on furthering our knowledge on the burning topic of Hypersonic flight.

Distribution is unlimited/AFRL-2023-2280; Cleared 05/11/2023